# Shotgun Transcriptome and Isothermal Profiling of SARS-CoV-2 Infection Reveals Unique Host Responses, Viral Diversification, and Drug Interactions

**Authors:**
Daniel J. Butler[1#], Christopher Mozsary[1#], Cem Meydan[1,2,3#], David Danko[1,4#], Jonathan Foox[1,2#], Joel Rosiene[5,6], Alon Shaiber[5,6,7], Ebrahim Afshinnekoo[1,2,3], Matthew MacKay[1], Fritz J. Sedlazeck[8], Nikolay A. Ivanov[1,2,9], Maria Sierra[1], Diana Pohle[10], Michael Zietz[11], Undina Gisladottir[11], Vijendra Ramlall[11,12], Craig D. Westover[1], Krista Ryon[1], Benjamin Young[1], Chandrima Bhattacharya[1], Phyllis Ruggiero[6], Bradley W. Langhorst[13], Nathan Tanner[13], Justyna Gawrys[6], Dmitry Meleshko[1,4], Dong Xu[14], Peter A. D. Steel[15], Amos J. Shemesh[15], Jenny Xiang[14,16], Jean Thierry-Mieg[17], Danielle Thierry-Mieg[17], Robert E. Schwartz[18], Angelika Iftner[10], Daniela Bezdan[10], John Sipley[6], Lin Cong[6], Arryn Craney[6], Priya Velu[6], Ari M. Melnick[18], Iman Hajirasouliha[1,2,7], Stacy M. Horner[19,20], Thomas Iftner[10], Mirella Salvatore[16], Massimo Loda[6], Lars F. Westblade[6,16], Melissa Cushing[6], Shawn Levy[21], Shixiu Wu[22,23], Nicholas Tatonetti[11], Marcin Imielinski[5,6,7*], Hanna Rennert[6*], Christopher E. Mason[1,2,3,24*]

**Affiliations:**
[1]Department of Physiology and Biophysics, Weill Cornell Medicine, NY, USA.
[2]The HRH Prince Alwaleed Bin Talal Bin Abdulaziz Alsaud Institute for Computational Biomedicine, Weill Cornell Medicine, NY, USA
[3]WorldQuant Initiative for Quantitative Prediction, Weill Cornell Medicine, NY, USA
[4]Tri-Institutional Computational Biol. & Medicine Program, Weill Cornell Medicine, NY, USA
[5]New York Genome Center, NY, USA
[6]Department of Pathology and Laboratory Medicine, Weill Cornell Medicine, NY, USA
[7]Englander Institute for Precision Medicine and the Meyer Cancer Center, Weill Cornell Medicine, NY, USA
[8]Human Genome Sequencing Center, Baylor College of Medicine, Houston, TX, USA
[9]Clinical & Translational Science Center, Weill Cornell Medicine, NY, USA
[10]Institute of Medical Virology and Epidemiology of Viral Diseases, University Hospital Tuebingen, Germany
[11]Department of Biomedical Informatics, Department of Systems Biology, Department of Medicine, Institute for Genomic Medicine, Columbia University, NY, USA
[12]Department of Cellular, Molecular Physiology & Biophysics, Columbia University, NY, USA
[13]New England Biolabs, MA, USA
[14]Genomics Resources Core Facility, Weill Cornell Medicine, NY, USA
[15]Department of Emergency Medicine, Weill Cornell Medicine, NY, USA
[16]Division of Infectious Diseases, Department of Medicine, Weill Cornell Medicine, NY, USA
[17]National Center for Biotechnology Information, National Library of Medicine, National Institute of Health, MD, USA
[18]Department of Medicine, Weill Cornell Medicine, NY, USA
[19]Department of Molecular Genetics and Microbiology, Duke University Medical Center, NC, USA
[20]Department of Medicine, Duke University Medical Center, NC, USA
[21]HudsonAlpha Discovery Institute, Huntsville, AL, USA
[22] Hangzhou Cancer Institute, Hangzhou Cancer Hospital, Hangzhou, China
[23]Department of Radiation Oncology, Hangzhou Cancer Hospital, Hangzhou, China

[24]The Feil Family Brain and Mind Research Institute, Weill Cornell Medicine, NY, USA
[#]These authors contributed equally to this work
*To whom correspondence should be addressed

**Corresponding Authors:**
Marcin Imielinski (mai9037@med.cornell.edu); Hanna Rennert (har2006@med.cornell.edu); Christopher E. Mason (chm2042@med.cornell.edu)

**Abstract**
The Severe Acute Respiratory Syndrome Coronavirus 2 (SARS-CoV-2) has caused thousands of deaths worldwide, including >18,000 in New York City (NYC) alone. The sudden emergence of this pandemic has highlighted a pressing clinical need for rapid, scalable diagnostics that can detect infection, interrogate strain evolution, and identify novel patient biomarkers. To address these challenges, we designed a fast (30-minute) colorimetric test (LAMP) for SARS-CoV-2 infection from naso/oropharyngeal swabs, plus a large-scale shotgun metatranscriptomics platform (total-RNA-seq) for host, bacterial, and viral profiling. We applied both technologies across 857 SARS-CoV-2 clinical specimens and 86 NYC subway samples, providing a broad molecular portrait of the COVID-19 NYC outbreak. Our results define new features of SARS-CoV-2 evolution, nominate a novel, NYC-enriched viral subclade, reveal specific host responses in interferon, ACE, hematological, and olfaction pathways, and examine risks associated with use of ACE inhibitors and angiotensin receptor blockers. Together, these findings have immediate applications to SARS-CoV-2 diagnostics, public health, and new therapeutic targets.

**Keywords**: severe acute respiratory syndrome coronavirus 2 (SARS-CoV-2), coronavirus disease 2019 (COVID-19), loop-mediated isothermal amplification (LAMP), quantitative reverse transcription polymerase chain reaction (qRT-PCR), next-generation sequencing (NGS), RNA-seq, global health.

## Introduction

In March 2020, the World Health Organization (WHO) declared a pandemic of the coronavirus disease 2019 (COVID-19), an infection caused by severe acute respiratory syndrome coronavirus 2 (SARS-CoV-2) (He *et al*., 2020). Since its start, more than three million of cases and more than two hundred of thousand deaths have been reported (https://coronavirus.jhu.edu), with an especially high burden in New York City (NYC). Since the presenting symptoms of COVID-19 can resemble those of common viral respiratory infections, a molecular diagnosis is required to reliably distinguish a SARS-CoV-2 infection from influenza and other respiratory illnesses (Guan *et al.,* 2020, Zhou *et al*., 2020).

The current gold standard (qRT-PCR-based) approaches to SARS-CoV-2 molecular testing are largely limited to hospital or academic laboratories and reserved for the most severe cases, with limited accessibility to the general public. As a result, the true prevalence of SARS-CoV-2 in the population is mostly unknown, particularly among pre-symptomatic, mild symptomatic, or asymptomatic cases. Though several novel, scalable biotechnological approaches for viral testing have recently emerged (e.g., CRISPR-Cas12a (Broughton *et al*., 2020) or CRISPR-Cas13 (Metsky *et al*., 2020) on paper-based detection systems, or loop-mediated isothermal amplification (LAMP) (Tanner *et al*., 2015, Zhang *et al.*, 2020, Yu *et al*., 2020, Schmid-Burgk

93 *et. al*., 2020), these have not been validated against gold-standard clinical assays or next-
94 generation sequencing (NGS).
95
96 The lack of widely available, rapid SARS-CoV-2 diagnostics has fundamentally limited the
97 public health approach to COVID-19, including hampering ability to implement contact tracing
98 and accurate estimation of infection fatality rates. In addition, the persistence of SARS-CoV-2
99 across a range of surfaces (van Doremalen *et al*., 2020) and hospital areas (Ong *et al.*, 2020)
100 raises the specter of COVID-19 spread via fomite transmission. A key question is whether the
101 environmental surface distribution of SARS-CoV-2 in high-touch, high-traffic areas (e.g.
102 subways) may have driven its rapid emergence in certain regions (e.g., NYC). As yet, little
103 information exists about RNA viruses in public areas.
104
105 Nonetheless, genomic viral surveillance resources, such as Global Initiative on Sharing All
106 Influenza Data (GISAID), the Johns Hopkins University (JHU) Dashboard, and Nextstrain
107 (https://nextstrain.org/ncov) (Gardy *et al*., 2015, Dong *et al*., 2020, Meyers *et al*., 2020, Hadfield
108 *et al*., 2018) have enabled dynamic tracking of patient-derived viral evolution during the
109 COVID-19 pandemic. These efforts still only cover a fraction (<0.5%) of documented cases,
110 motivating ongoing viral profiling efforts. Unlike the results of simple binary diagnostic tests,
111 full-length viral genome sequences can reveal patterns of strain evolution, temporal and
112 geographic trajectories of viral spread, and correlations between specific genotypes and clinical
113 features (e.g. disease severity, comorbidities, and viral load). These genomic epidemiology
114 efforts have already played a crucial public health role in confirming community spread of
115 SARS-CoV-2 in the USA (Zhao *et al*., 2020, Gonzalez-Reiche *et al*., 2020, Fauver *et al*., 2020)
116 as well as in China (Lu *et al*., 2020). However, standard approaches to viral profiling (i.e.
117 targeted sequencing) fail to provide information on either the host immune response or microbial
118 co-infections, both which might impact the clinical presentation of COVID-19 and provide
119 directions for therapeutic intervention and management.
120
121 To address these gaps in knowledge of disease and technology, we designed and validated a
122 rapid reverse transcriptase LAMP (RT-LAMP) assay to detect SARS-CoV-2 infection from
123 nasopharyngeal swab specimens and oropharyngeal swab lysates. We then integrated this assay
124 into a large-scale host and viral profiling platform that combines targeted diagnostics with
125 shotgun metatranscriptomics (**Figure 1a**). We applied this total RNA-seq platform to 857
126 samples from 735 confirmed or suspected COVID-19 cases at New York-Presbyterian Hospital-
127 Weill Cornell Medical Center (NYPH-WCMC) and 86 environmental samples collected from
128 high-transit areas in the NYC subway in early March 2020. Our results define genetic features of
129 the NYC outbreak and implicate specific host responses in SARS-CoV-2 infection, including
130 perturbations of the angiotensin converting enzyme (ACE) pathway.
131
132 **Results**
133
134 ***Rapid, single tube detection of SARS-CoV-2***
135 We developed a colorimetric assay to quickly detect and quantify SARS-CoV-2 viral load in
136 patient and environmental samples, utilizing a set of six LAMP primers and simple single tube
137 protocol (**Figure 1a-b**). Primers were designed to create two nested loops and amplify within the
138 SARS-CoV-2 nucleocapsid gene (N gene), which enabled a 30-minute reaction workflow.

139 Related pathogens, high prevalence disease agents, and normal or pathogenic microbiota that are
140 reasonably likely to be encountered in the clinical samples were evaluated to identify the percent
141 homology between the primer sequences and these other organisms, and the probes were also
142 designed to avoid known polymorphisms (see Methods).
143
144 To validate the assay, we first evaluated two synthetic RNAs (see Methods) whose sequences
145 matched the viral sequences of patients from Wuhan, China and Melbourne, Australia (**Supp.**
146 **Fig. 1**). The first control (MT007544.1) was used to test the analytical sensitivity via the limit of
147 detection (LoD), titrated from 1 million molecules of virus ($10^6$) down to a single copy, using
148 serial $\log_{10}$ dilutions. The reaction output was measured at 0-, 20-, and 30-minute intervals
149 (**Figure 1c, Supp. Figure 2a**) before the samples were heated to 95ºC for inactivation. LAMP
150 fluorescence correlated closely with SARS-CoV-2 RNA viral copies (**Figure 1d**), with an
151 overlap of the median signal from negative controls at lower levels (0-10 total copies per
152 reaction) of viral RNA (n=10). The LoD was found to be between 5–25 viral total copies for the
153 dual primer, single-tube reaction (N gene and E gene), and this was then replicated to show a
154 similar LoD on the second synthetic control from a patient from Wuhan (**Supp. Figure 2b, 3a**).
155
156 To optimize the LAMP assay for clinical samples, we first tested the reaction on a range of
157 sample types, dilutions, and reaction volumes. We used a set of 201 samples from known or
158 suspected COVID-19 cases that were tested for SARS-CoV-2 by a commercial qRT-PCR assay
159 that has been the primary clinical test at NYPH-WCMC since early March. These comprised 69
160 nasopharyngeal (NP) swab samples that tested positive (qRT-PCR positives, Ct<40) and 132
161 samples that tested negative (qRT-PCR negative, Ct ≥ 40) (see Methods). qRT-PCR positive
162 samples showed a much higher LAMP fluorescence than qRT-PCR negative samples, with
163 superior performance observed at higher (10µL vs 5µL) input volumes (**Supp. Figure 3b**). qRT-
164 PCR positive samples that failed to generate LAMP fluorescence were associated with lower
165 viral genome abundance (high cycle threshold [Ct] value qRT-PCR). We obtained similar
166 performance on bulk oropharyngeal swab lysate (**Supp. Figure 3c-e**), including increasing
167 reaction sensitivity as a function of viral copy number. This lysate protocol required only a 30-
168 minute lysis time for the oral collections and 30-minute LAMP reaction time. These results
169 indicate robust performance of the LAMP assay across a broad range of purified nucleic acids as
170 well as crude cellular lysates (see Methods).
171
172 Analysis of Receiver Operator Characteristic (ROC) curves revealed an optimal threshold of
173 11,140 QuantiFluor relative fluorescence units (RFUs), which yielded an overall sensitivity of
174 95.6% and specificity of 99.2% (**Figure 1e**). We observed higher LAMP sensitivity at higher
175 viral loads, as determined by qRT-PCR Ct values (**Supp. Fig. 4**). The highest viral load (Ct <20)
176 showed 100.0% sensitivity and 97.4% specificity, compared with the sensitivity at the lowest
177 viral load at 80.0% (Ct >28, RFU below 7010). These same LAMP assay thresholds yielded
178 consistent test positivity for synthetic RNA positive controls (Twist Biosciences) as well as
179 clinical spike-in carrier RNAs (20/20) (**Supp. Fig. 4**), and consistent signal from clinical viral
180 positives in Vero E6 cells (100.0%, 12/12) and blank clinical buffer negatives (100.0% 8/8).
181
182 ***Shotgun metatranscriptomics platform for viral, microbiome, and host genomics***
183 To provide orthogonal validation of our LAMP assay and further investigate the biological
184 characteristics of qRT-PCR positive and negative specimens, we developed a shotgun

185 metatranscriptomics platform utilizing total RNA-seq (RNA-sequencing with ribosomal RNA
186 depletion) to profile all RNAs from patient and environmental swab specimens (**Figure 1a**). We
187 sequenced 857 RNA-seq libraries (**Figure 2**) across 735 COVID-19 cases and controls
188 (including the 201 tested with LAMP) to an average of 63.2M read pairs per sample. This
189 spanned 243 qRT-PCR positive and 546 qRT-PCR negative samples, 17 positive controls (Vero
190 E6 cells), and 33 negative controls (buffer). Replicate RNA-seq libraries from clinical samples
191 were merged into a final set of 216 qRT-PCR positive samples and 519 qRT-PCR-negatives.
192
193 We aligned total RNA-seq reads to the human genome and NCBI reference databases (see
194 methods), Kraken2 classification of non-human sequences revealed abundant bacterial or SARS-
195 CoV-2 RNA alignments, with a lower proportion of sequences mapping to fungi, archaea, or
196 other viruses (**Figure 2a**). Positive controls and clinical samples demonstrating qRT-PCR Ct
197 values consistent with medium and high viral loads were significantly ($p < 1 \times 10^{-16}$) enriched in
198 SARS-CoV-2 genome alignments (median reads per kilobase per million mapped reads, RPKM)
199 relative to negative controls and qRT-PCR negative clinical samples (**Figure 2b**). A comparison
200 of LAMP fluorescence, qRT-PCR Ct values, and total-RNA Seq RPKM across 201 clinical
201 specimens demonstrated consistent estimates of SARS-CoV-2 viral abundance across these three
202 technologies ($R_{seq_vs_Ct} = -0.84$, $R_{seq_vs_lamp} = 0.82$, $R_{lamp_vs_Ct} = -0.80$) (**Figure 2c, Supp. Figure**
203 **5a**), as well as RNA-seq extraction replicates (**Supp. Figure 5b**). These results provide
204 additional validation for the LAMP SARS-CoV-2 assay on clinical samples.
205
206 Analysis of total RNA-seq sequences also enabled mapping of likely co-infections and
207 colonization with commensal species across both clinical positives and negatives in our sample
208 set. We identified additional RNA viruses and organisms that distinguished high, medium, and
209 lower viral load patients (**Supp Table 1, Supp. Figure 6**), with overall similarity observed
210 across patients in the bacterial RNA fractions (**Supp. Figure 7a)**. However, other known
211 respiratory viruses were observed in some of the COVID-19-positive patients (3.2%), including
212 human coronaviruses 229E, coronaviruses NL63, influenza A, and human mastadenovirus and
213 metapneumovirus (**Supp. Figure 7a)**. Most patients (209/216, 96.8%) that presented with the
214 SARS-CoV-2 virus showed no evidence of other respiratory viruses, although bacterial mapping
215 showed 102 patients with reads mapping to *Mycoplasma pneumonia* (relative abundance >
216 0.01%) (**Supp. Table 1**).
217
218 ***Environmental sampling of SARS-CoV-2 in the NYC subway***
219 Having validated a rapid LAMP assay and shotgun metatranscriptomics platform, we next
220 investigated the environmental distribution of SARS-CoV-2 in high-transit areas of the NYC
221 subway at the beginning of the NYC pandemic. We collected 62 samples from handrails, kiosks,
222 and floors in Grand Central and Times Square subway stations between March 6 and 13th, 2020
223 and generated 86 RNA-seq libraries. Each sample was collected using a sterile and DNA/RNA
224 free swab, following the MetaSUB sampling protocols for nucleic acid stabilization (Danko *et*
225 *al*., 2020).
226
227 To further investigate these 86 environmental samples for the presence of SARS-CoV-2, we
228 generated total RNA-seq libraries and investigated the distribution of non-human sequences.
229 These samples demonstrated a mix of fungal and archaeal species that was consistent with
230 underground subway origin (Danko *et al*., 2020) (**Supp. Table 1**). However, we did not observe

231 significant counts or proportions (**Figure 3a**) of SARS-CoV-2 reads, which was particularly
232 clear with dual-index library preparations (**Supp. Figure 8**). However, a broad range of other
233 bacterial and viral species was found, including a large set of phages (e.g. *Streptomyces* phage
234 VWB), desiccation-tolerant bacteria (e.g *Deinococcus radiodurans*), and more abundant
235 bacterial and archaeal RNA than the clinical samples (**Supp. Table 1**). Of note, these were
236 checked against a database of putative false positives (**Supp. Table 2**), which was created from
237 *in silico* fragmentation of the SARS-CoV-2 genome and mapping against the same database.
238 Taken together, these results indicate that high transit surfaces were not likely to harbor
239 significant levels of SARS-CoV-2 in the early phases of the NYC epidemic.
240
241 ***SARS-CoV-2 assemblies from shotgun metatranscriptomes***
242 The abundance of SARS-CoV-2 alignments from total RNA-seq was sufficient to provide >10x
243 coverage of the viral genomes and yield high quality, full-length assemblies for 155 samples,
244 including 146 (67.6%) of qRT-PCR positive patient samples (**Figure 3a, Supp. Figure 6**). The
245 97 qRT-PCR positive samples that yielded partial or no assembly demonstrated low or uneven
246 genome-wide read depth, though these were increased on average relative to qRT-PCR
247 negatives. We also generated full length SARS-CoV-2 assemblies for 9 samples that were found
248 negative by qRT-PCR (**Figure 3a**). Each of these demonstrated a high RPKM viral load, an
249 abundance of reads evenly covering the SARS-CoV-2 genome, and high (>0.5) variant allele
250 fractions (VAFs) of SNV's commonly seen in positive samples, as well as a recent build of
251 GISAID (**Figure 3b**). Apart from these common variant sites, we did not find additional
252 recurrent mutations that might explain why these cases were not detected by qRT-PCR (e.g.
253 primer site mutation).
254
255 When examining the viral genomes, we identified a total of 1,147 instances of 165 unique
256 variants across 155 assemblies, including 1,143 single nucleotide variants (SNVs) and 4
257 deletions. Variant calling of assemblies and RNA-seq reference alignments showed most
258 (87.5%) variants with VAFs >0.95 and high (>100) numbers of variant-supporting reads.
259 Analysis of VAF posterior probability distributions identified a subset of alleles whose VAFs
260 were confidently (probability > 0.95) above 0.05 but below 0.95. We labeled these alleles as
261 "het" (heterogenous) variants and refer to the remaining (high VAF) consensus assembly variants
262 as "homogeneous." Many of these het variants were associated with robust read support despite
263 frequently having VAFs below 0.5 and not being incorporated into the consensus assembly
264 sequence. A subset of samples (11/155) samples harbored at least 5 het variants, with a
265 significant enrichment (P = 0.0054) in qRT-PCR negative cases (**Figure 3c**). Analyzing the
266 population allele frequencies (PAF) of these het variants across GISAID revealed the vast
267 majority (91%) to be rare (PAF<0.1) or even private to that sample, indicating that these were
268 unlikely to be due to cross contamination (**Figure 3d**).
269
270 We then asked whether het variants might indicate the presence of a viral subclone, arising either
271 through co-infection or intra-host adaptation. Analyzing het-rich (>5 het variants) samples,
272 revealed that set of het variants observed in a single sample showed similar VAFs, yielding clear
273 peaks when summing their individual posterior probability densities (**Figure 3e**). These results
274 were consistent with the presence of a viral subclone at some fraction *f* corresponding to the
275 modes of each of these VAF distributions (0.1-0.2). Interestingly, each of the three samples
276 shown in **Figure 3e** also harbored a clear peak of homogenous variants with VAFs near 1. These

277 results suggest that the viral subclone is not the result of a coinfection by two viruses, which
278 would yield a second peak at 1-*f* at every major clone variant that has the reference allele in the
279 minor subclone. Het variants were found to occur at common sites of consensus variants across
280 samples, however, rare private hets were also present (**Figure 3f**).
281
282 ***Global phylogenetic relationship of NYC strains***
283 We next integrated 141 full-length NYPH-WCMC sequences with 7,806 SARS-CoV-2
284 sequences obtained from a recent GISAID build (downloaded on 4/20/2020) into a maximum
285 likelihood phylogenetic tree using the Nextstrain algorithm (Hadfield *et al*., 2018) (**Figure 4a**,
286 see Methods**)**. This integration resulted in 141/155 NYPH-WCMC sequences integrated into the
287 tree. Analyzing worldwide groupings annotated by the Nextstrain database, we found a high
288 proportion (>87%, 123/141) of incorporated samples were associated with A2, a large Western
289 European-derived clade that comprises nearly half of the sequences in GISAID, which agrees
290 with recently published findings (Gonzalez-Reiche *et al*., 2020). In addition, we found a minority
291 of samples from clades with mixed Asian and European origins (A1a, 6% of cases; B1, 4% of
292 cases; B, 3% of cases). Among these, we identified a clear predominance (94.1%, 146/155) of
293 the "L" strain, which is defined by a reference base at position 28143 (ORF8) and previously
294 associated with severe cases in Wuhan (Tang *et al*., 2020) (**Figure 4b**).
295
296 Among the A2 cases in our cohort, we found a recurrent 9 bp in-frame deletion (g.686_694del)
297 in the gene encoding non-structural protein 1 (NSP1). NSP1 is a putative SARS-CoV-2 virulence
298 factor that is highly divergent across betacoronaviruses (Narayanan *et al.,* 2015). This deletion
299 was assembled in 3 of 93 NYPH-WCMC samples, in which it showed robust read support with
300 near >0.95 VAF across thousands of high-quality alignments to the locus (**Figure 4c**). An
301 identical deletion was observed in 15 other samples in the GISAID database, spanning samples
302 from England, Iceland, and Canada, as well as three additional cases from New York. Among
303 these, 12 of 15 were labeled as part of clade A2 by Nextstrain, while two (Washington state)
304 cases were associated with a distant clade B1 (**Figure 4d**). This deletion removes three amino
305 acids (p.141_143KSD), including a residue that is variant (143Y>F) relative to the SARS-CoV-1
306 genome (**Figure 4c**). Interestingly, a 16th case (Washington, clade A2, **Figure 4c**) showed a
307 related but not identical 9 bp in-frame deletion (g.686_694del) that removes the same three
308 residues. These residues occur in a conserved portion of the C-terminal region of NSP1, which
309 has been linked to host chemokine dysregulation and translational inhibition in SARS-CoV
310 (Narayanan *et al.,* 2015).
311
312 ***A novel SARS-CoV-2 subclade enriched in NYC cases***
313 Given the predominance of clade A2 among NYC cases, we next asked whether specific variants
314 were enriched in NYC A2 samples relative to other regions' A2 samples. Comparing variant
315 frequencies between A2 cases in our data and non-NYC cases in GISAID, we identified six
316 enriched loci with FDR<0.1 (Fisher's exact test, one-tailed) that were over-represented in NYC
317 A2 samples (**Figure 5a**). All six of these variants were significantly enriched (Bonferroni-
318 adjusted p-value <0.05) in a second analysis comparing all other cases from NYC in GISAID vs.
319 the rest of the world (**Figure 5a**). Visualizing the most significant of these variants across the
320 Nextstrain derived phylogenetic tree (**Figure 5b**) demonstrated that the highest frequency of
321 these variants (25563G>T), defined a novel subclade of A2, which we call A2-25563. This
322 subclade comprised 84.4% (572/678) of (NYPH-WCMC and GISAID) NYC samples, and

323 92.7% (572/617) of the A2 portion of NYC cases (Sinai and NYU). Interestingly, while all three
324 of the NYPH-WCMC A2 cases harboring the aforementioned NSP1 9-bp deletion were in A2-
325 25563, many of the remaining cases were distributed across other subclades. Unlike the SNVs
326 used to define A2-25563, this deletion appeared to be highly polyphyletic with 7 unique
327 phylogenetic clusters associated with the deletion across a variety of clades (**Figure 4c**, **Figure**
328 **5b**).
329
330 Investigating the geographical and temporal distribution of non-NYC samples in A2-25563, we
331 found a global distribution with likely origin in Western Europe (**Figure 5c, 5d**). The first noted
332 case of A2-25563 in GISAID was in Belgium on 2/21/2020, but since then, this putative
333 subclade has represented a minority (20%) of Western European cases. While the prevalence of
334 A2-25563 in NYC appeared to be consistently high across sampling dates, it constituted only a
335 moderate proportion of cases from the Western and (non-New York portion of the) Eastern USA
336 (<50%) in early March (**Figure 5d**). Strikingly, we found that of the prevalence of the A2-25563
337 clade across Eastern and Western United States steadily and significantly increased through late
338 March and early April, while remaining stable in the Midwest. Among the early locations
339 showing high fractions of A2-25563 was West Africa, which has steadily decreased in
340 prevalence since early March (**Figure 5d**). The SNVs defining A2-25563 subclade were non-
341 synonymous variants targeting genes encoding the non-structural protein 2 (NSP2), the viral
342 replicase, and ORF3a, a poorly characterized SARS-CoV-2 protein with putative roles in
343 inflammation (Siu *et al.*, 2019). This subclade defining ORF3a site (p.Gln57His) is distinct from
344 that which defines the previously characterized L strain (p.Leu84Ser) (Tang *et al*., 2020).
345
346 ***Defining the SARS-CoV-2 host transcriptome***
347 We leveraged the comprehensive nature of the total RNA-seq profiles to better understand the
348 host transcriptome during SARS-CoV-2 infection. Cell proportion analyses using the MUSIC
349 deconvolution algorithm showed enriched proportions of cell types spanning goblet, ciliated
350 airway, and epithelial cells across all samples (**Supp. Figure 9**). Differentially expressed genes
351 (DEGs) associated with SARS-CoV-2 infection were calculated using limma voom and DESeq2
352 (see Methods). Overall, 757 significant DEGs ($q<0.01$, >1.5-fold change) were found the qRT-
353 PCR positive vs. negative samples (**Supp. Table 3)**, spanning 350 up-regulated DEGs and 407
354 down-regulated DEGs, and a total of 8851 unique genes ($q<0.01$, >1.5-fold change) across
355 different subgroups including a subset that were distinct from other detected viral respiratory
356 infections (**Figure 6a, Supp. Figure 12**). These spanned viral response pathways, innate immune
357 response, and interferon signaling (**Figure 6b,d, Supp. Figure 10a**), but also included iron,
358 olfaction, calcium, and ribosome dysregulation.
359
360 Differentially expressed host genes indicated a wide range of antiviral responses, including a
361 common interferon response across all ranges of viral levels, which was significantly higher
362 when compared to SARS-CoV-2 negative samples that harbored other respiratory viruses
363 (**Figure 6a,b**). Notably, host cells showed an increase in angiotensin converting enzyme 2
364 (*ACE2)* expression (**Figure 6b**) (p-value=$1.4\times10^{-9}$), which is the SARS-CoV-2 cellular receptor
365 (Hoffmann *et al*., 2020). This critical gene for viral entry (Sungnak *et al*., 2020) exhibited a
366 dose-dependent expression concomitant with the higher levels of SARS-CoV-2 virus, along with
367 IFI27 (Interferon Alpha Inducible Protein 27, $p < 2.2\times10^{-16}$) and IFI6 (Interferon Alpha Inducible
368 Protein 6, $p < 2.2\times10^{-16}$). The DEGs also included HERC6 (HECT Containing E3 Ubiquitin

369 Protein Ligase Family Member 6), which aids Class I MHC-mediated antigen processing and
370 Interferon-Stimulated Genes (ISGs) (**Figure 6b,c,d**), underscoring the impact of the virus on
371 these cells' immune response (Oudshoorn *et al*., 2012). Also, a subset of cytokines (CXCL10,
372 CXCL11, CCL8) showed the highest spike of expression in the higher viral load sub-group
373 (**Supp. Figure 10**), matching previous results from animal models and infected cells (Blanco-
374 Melo *et al*., 2020). The host transcriptome that exhibited the greatest amount of DEGs were
375 those with the highest viral titer (**Figure 6a**).
376
377 Down-regulated genes and those with a negative enrichment score (NES) were functionally
378 distinct (**Figure 6d**). This included a significant decrease in gene expression for the olfactory
379 receptor pathway genes (q-value =0.0005, **Supp. Table 4**), which is consistent with a COVID-19
380 phenotype wherein patients lose their sense of smell. Other down-regulated genes included the
381 transmembrane serine protease *TMPRSS-11B,* which regulates lung cell growth (Updegraff *et al*.,
382 2018) and *ALAS2*, a gene which makes erythroid ALA-synthase (Ajioka *et al*,. 2006) that is
383 found in developing erythroblasts (red blood cells). ALA-synthase plays an important role in the
384 production of heme TRIM2 E3 ubiquitin ligase induced during late erythropoiesis, which
385 indicated a connection to hematological and iron (heme) regulation during infection (**Figure 6d**).
386 Accordingly, genes in a related biological network were significantly enriched based on Gene
387 Ontology (GO) pathways for iron regulation (q-value 0.04, **Supp. Table 4**). Both the up-
388 regulated and down-regulated gene expression differences in were distinct from those of house-
389 keeping genes (**Supp. Figure 11**), which stayed mostly stable during infection.
390
391 ***ACE inhibitor/angiotensin receptor blocker usage correlates with COVID-19***
392 Finally, given our observation of increased *ACE2* gene expression in patients with high SARS-
393 CoV-2 viral load, we then investigated the interplay of receiving pharmacologic angiotensin
394 converting enzyme inhibition (ACEI) or angiotensin receptor blockers (ARBs) for hypertension
395 and clinical features of COVID-19 disease. Since *ACE2* expression can be increased in patients
396 taking ACEIs and ARBs (Agata *et al*., 2006), the observed correlation of viral titer with *ACE2*
397 expression may be attributed to the pre-infection use of such inhibitors, which is common in
398 older patients and those with comorbidities (Fang *et al*., 2020). To address this, we analyzed an
399 observational cohort of 8,856 patients with suspected SARS-CoV-2 infection from New York
400 Presbyterian Hospital-Columbia University Irving Medical Center (NYPH-CUIMC) for their
401 usage of ACEIs and ARBs (4,829 who tested positive). We found that use of ACEIs/ARBs was
402 strongly associated with testing positive in patients suspected of SARS-CoV-2 infection (Odds
403 Ratio, OR=2.7, and 95% Confidence Interval, CI=2.2-3.94, p=7.43E-28, **Figure 6e**). This result
404 was consistent when corrected for age, sex, and IL-6 (OR=1.5 CI:1.2-1.8), when corrected for
405 comorbidities (**Table 1**) (OR=1.754 CI:1.4-2.0) and when only considering patients with
406 hypertension (OR=1.8, CI: 1.4-2.3). For comparison, we repeated this analysis with calcium
407 channel blockers (CCBs), another class of anti-hypertensives, and found no association between
408 CCB exposure and infection. We found that patients with hypertension who take ACEIs and
409 ARBs have higher infection rates than patients with hypertension on CCBs (OR=1.5 CI: 1.2-2.0,
410 p=0.0011) (**Table 2**).
411
412 We found a range of effects when investigating the relationship between ACEI/ARB usage and
413 morbidity and mortality. In an uncorrected univariate analysis, ACEI/ARB usage conferred an
414 increased risk of intubation and mortality for SARS-CoV-2 positive patients (intubation: HR=2.8

CI:2.3-3.5, 6.99E-24) (**Figure 6e** and **Figure 6f**) and mortality: HR=2.2 CI:1.8-2.7, p=3.18E-14 (**Figure 6e** and **Figure 6g**). These results hold when correct for age, sex, and IL6 (**Figure 6e**). However, when correcting for comorbidities, only intubation was significant (HR=1.7 CI:1.4-2.2, p=5.91E-07). Further, in the analysis where only patients with hypertension were included, we found modest evidence for both (i) a risk of intubation in the univariate model (HR=1.4 CI:1.1-1.8, p=0.02) and (ii) a protective effect of ACEI/ARBs for mortality in the covariate models (HR=0.8 CI:0.6-1.0, p=0.03).

Additionally, we confirmed previously reported risk factors for both mechanical respiration and mortality. For requirement of mechanical respiration, we found significant risk effects from male sex (p=2.76E-03), diabetes (p=2.64E-02), and IL-6 (p=1.07E-121). In addition, for mortality we found significant effects from age (p=1.10E-86), male sex (p=1.98E-04), diabetes (p=6.04E-04), being overweight (p=3.86E-03), and IL-6 (p=8.68E-23). Finally, in a post-hoc comparative analysis between specific ACEIs, we found no significant differences in infection rates, intubation, or mortality with any single ACEI drug over another (**Supp. Figure 13)**. In a similar analysis on ARBs, we found that olmesartan was associated with an increased risk of mortality (HR=2.3 CI: 1.1-4.9, p=0.03, N=28) in the hypertension-only analysis. We found no risk in the larger cohort nor for any other single ARB (**Supp. Figure 13**, with complete modeling results are provided in **Supplemental Tables 6-9**).

***Discussion***

During a large-scale pandemic with exponential spread, such as COVID-19, scalable methods for diagnosis and screening are crucial for both mitigation and containment (Lan *et al*., 2020, Liu *et al*., 2020). While hospital-grade, core lab devices can achieve massive throughput (thousands of samples per day), a key limitation of these assays is accessibility of testing facilities to patients, the logistics of sample transport, and timely test reporting. These limitations become even more stark in the context of widespread quarantines and nationwide lockdowns, where requiring patients to travel (even for viral testing) incurs significant personal and public health risks.

The most urgent diagnostic need in this situation is for scalable rapid point-of-care tests that can be potentially implemented in the home. Our validation of a rapid one-tube, dual-primer colorimetric SARS-CoV-2 assay with both qRT-PCR and total RNA-seq provides a potential solution to this problem. Further work will be needed to assess whether this LAMP assay can detect the presence of SARS-CoV-2 at even lower (but clinically relevant) viral concentrations in specimen types that are less cumbersome to collect than naso/oropharyngeal swabs (e.g. saliva, stool). As we demonstrate, this LAMP SARS-CoV-2 assay can be also applied for environmental sampling, which may be crucial in the containment and recovery phases of this pandemic. Specifically, LAMP positivity may quickly indicate if an area is infectious and a negative result (with appropriate confirmation) will possibly represent a lower risk. Indeed, these tools and methods can help create a viral “weather report” if broadly used and partnered with continual validation.

Total RNA-sequencing data enabled a complete genetic map of the viruses in a significant subset of our samples. Remarkably, we found 9 qRT-PCR negative cases among the 155 cases that had sufficient reads to assemble the SARS-CoV-2 genome *de novo*. Though these likely qRT-PCR false negatives could not be attributed to specific sequence changes (e.g. primer site mutations),

461 their high frequency underscores the limitation of "gold standard" qRT-PCR approaches for
462 SARS-CoV-2 detection. These results further highlight the need for open-source primer design
463 (the RT-PCR methods for this FDA-approved test are proprietary), so these assays can be
464 updated as a more granular picture of strain diversity and evolution is obtained through
465 worldwide sequence efforts.
466
467 Notably, our phylogenetic analysis nominates an A2 subclade (A2-25563, defined by
468 25563G>T) which comprises the majority of known NYC samples, including those sequenced
469 outside of this study (Gonzalez-Reiche *et al.*, 2020). Though remaining NYC cases show a wide
470 distribution across all identified clades, the predominance (>80% in NYC) of such a narrowly
471 defined set of sequences within NYC from a rare (≤20%) Western European subclade is striking.
472 The steady increase of A2-25563 prevalence in other regions in the Eastern and Western USA
473 (but not Midwest) through late March and early April may be consistent with emigration patterns
474 of NYC residents who left the city during the lockdown. The dominance of the proposed A2-
475 25563 subclade in NYC suggests either (1) a very early introduction by a single patient
476 harboring A2-25563; or (2) multiple A2-25563 founder events; or (3) disproportionate
477 community transmission of strains within this subclade. The first possibility may be potentially
478 linked to expansion among cases in the New Rochelle cluster, though additional genotyping
479 and/or metadata aggregation from those sequenced cases would be required to assess this
480 hypothesis. The third possibility could be consistent with A2-25563 harboring differential
481 fitness with respect to transmissibility or virulence relative to other A2 viruses.
482
483 Future studies correlating viral genotypes with patient outcomes in larger cohorts will be
484 necessary to determine whether any of these A2-25563 associated variants functionally influence
485 viral transmission or disease severity. The polyphyletic pattern and convergent evolution pattern
486 observed with NSP1 p.141_143KSD, including clades outside of A2, raises the possibility that
487 this variant arose multiple times and may be under positive selection. Given the small number of
488 these variants observed in our analysis (14), larger and more statistically powered datasets will
489 be required to evaluate this hypothesis. The VAF distribution in patients harboring het variants
490 suggests that intrahost diversification may lead to the development of SARS-CoV-2 subclones in
491 a subset of COVID-19 cases. The relatively large numbers of these het variants (>10)
492 presumably arising during the course of a single infection rising to a reasonably high oligoclonal
493 VAFs (0.1-0.2) suggests that this intrahost diversification may be rapid and also associated with
494 positive selection.
495
496 Our results demonstrate that distinct host transcriptional programs are activated during viral
497 infection of the naso-/oropharynx with SARS-CoV-2. This includes upregulation of specific
498 interferon pathway genes (*SHFL*, *IFI6*, *IFI27*, and *IFIT1*). that have been previously associated
499 with the innate antiviral host immune response against other positive-strand RNA viruses (e.g.
500 hepatitis C, Dengue virus). These results provide clinical relevance for recently published results
501 from animal and cellular models of SARS-CoV-2 (Blanco-Melo *et al*., 2020). Our analyses also
502 implicate expression perturbations of the ACE pathway in SARS-CoV-2 host response, including
503 *ACE2*. ACE2 is the cognate cellular receptor for SARS-CoV and SARS-CoV-2 coronaviruses,
504 and a recently proposed drug target for SARS-CoV-2 (Monteil *et al.*, 2020). Patients presenting
505 with COVID-19 frequently harbor comorbidities such as hypertension, diabetes mellitus, and
506 coronary heart diseases, all which have been associated with increased disease severity (Fang *et*

507 *al*., 2020, Ferrario *et al*., 2005). Since these comorbidities are frequently treated with ACE
508 pathway perturbing medications (ACEIs and ARBs), one possibility is that these medications
509 may make patients more susceptible to SARS-CoV-2 infection.
510
511 Though previous epidemiological studies have reported increased mortality and morbidity in
512 COVID-19 patients with hypertension, we sought to examine this risk in the context of ACEI or
513 ARB use (Patel and Verma, 2020). Our retrospective clinical analysis shows that ACEI/ARB
514 exposure increased COVID-19 risk, but showed equivocal effects for morbidity and mortality
515 when conditioning on hypertension status. A recent study reported a protective effect of
516 ACEI/ARB exposure on mortality (Zhang *et al*., 2020). We were able to replicate their result by
517 conditioning on hypertension. However, this same analysis also revealed no effect, or possibly
518 even a risk, from ACEI/ARB exposure on mechanical respiration and a strong risk of infection.
519 Further, the association with infection was consistent regardless of conditioning on hypertension
520 and in a direct comparison to CCB exposure, mitigating some of the concerns about confounding
521 risk. Taken together, the results from these studies suggest caution should be taken before any
522 clinical guidelines are put in place. Prospective clinical trials or multi-centered blinded studies
523 may be necessary before more concrete conclusions can be drawn. For example, if some patients
524 are more susceptible because they are already expressing high levels of *ACE2*, this could help
525 with targeting ACE2 in these patients as a prophylactic method. However, if the cells respond to
526 infection with *ACE2* expression, and this leads to the cytokine storm seen in patients, then this
527 could be used as a downstream treatment (post-infection), for when ACE2 interacts with
528 TMPRSS2, such as the ongoing trials with camostat mesylate (Hoffman *et al*., 2020).
529
530 Finally, it is notable that the majority of the testing for SARS-CoV-2 so far has relied on
531 nasopharyngeal specimen collection, yet preliminary results here and elsewhere demonstrate
532 SARS-CoV-2 detection from oral specimens is feasible and likely optimal (Woelfel *et al*., 2020,
533 Wylie et al., 2020). Further studies comparing nasopharyngeal, oropharyngeal, buccal, and saliva
534 collection approaches, as well as a comparison of different swab types, are needed. Depending
535 on the availability of reagents and resources, as well as automation, a LAMP-based approach on
536 such sample types could allow facilities to increase testing capabilities by orders of magnitude.
537 Since viral pandemics can have significant, long-lasting detrimental impacts for affected
538 countries, it is crucial to deploy methods that can track and profile cases (e.g. RNA-seq, LAMP,
539 qRT-PCR) and provide a comprehensive view of host and viral biology. These methods can help
540 mitigate the medical and socioeconomic harm from viral outbreaks, as well as establish
541 protective surveillance networks that can help defend against future pandemics.
542
543 **Acknowledgements**
544 We thank the Core Facilities at Weill Cornell Medicine, the Clinical Laboratories at New York
545 Presbyterian Hospital, the Scientific Computing Unit (SCU), OneCodex, the XSEDE
546 Supercomputing Resources and the GISAID Initiative curators and submitters (**Supp Table 10**).
547 We also thank New England Biolabs for providing the reagents for preliminary testing of the
548 LAMP protocols, as well as Eileen Dimalanta and Ted Davis for technical discussions. The
549 authors wish to thank the following members of the HudsonAlpha Discovery team who
550 supported the RNASeq experiments described in the manuscript: Colleen Cowan, John Mote,
551 Arianna Pionzio, Melanie Robinson, and Madison Robison.
552

**Funding**
We are grateful for support from the STARR Foundation (I13-0052) the Vallee Foundation, the WorldQuant Foundation, The Pershing Square Sohn Cancer Research Alliance, Citadel, the National Institutes of Health (R01MH117406, R25EB020393, R01AI151059), the Bill and Melinda Gates Foundation (OPP1151054), the NSF (1840275), the National Center for Advancing Translational Sciences of the National Institutes of Health (UL1TR000457, CTSC), and the Alfred P. Sloan Foundation (G-2015-13964). FJS supported by the National Institute of Allergy and Infectious Diseases (1U19AI144297-01). MZ supported by T15LM007079. NPT and UOG supported by R35GM131905. NAI was supported by the National Center for Advancing Translational Sciences of the National Institutes of Health under Award Number TL1TR002386.

**Author Contributions**
CEM led the study design and coordination and HR led the clinical collection and validation work in the NYP CLIA laboratory, as well as with MI. Overall supervision and protocol development and implementation for the Zymo RNAClean and NEB assays (SL). DB and CMz performed the LAMP experiments to validate the assay, established a method to quantify LAMP output, and developed a protocol for clinical use of the assay. CW, DX, PR, JG, and JX assisted with sample preparation and sequencing. CeM, DD, JF, AS, JR, MM, EA, IH, DM, MI, BWL, MZ, UG, NPT, NAI, CEM performed analyses. DD, CMz, NAI, MS, BY, KR, CB coordinated and collected environmental samples. EA submitted the IRB application and helped with clinical coordination. Help and insights for analysis from EA, SL, MI, MS, LFW, ML, MC, HR, KR all led to the figures and analyses. All authors reviewed, edited, and approved the manuscript.

**Conflicts of Interest**
Nathan Tanner and Bradley W. Langhorst are employees at New England Biolabs.

**IRB**
Samples were collected and processed through the Weill Cornell Medicine Institutional Review Board (IRB) Protocol 19-11021069. Observational cohort analysis (ACEI/ARB) was done through the Columbia University IRB Protocol AAAL0601.

**Data Accessibility**
Viral sequences were uploaded into GISAID (Global Initiative on Sharing All Influenza Data) site (https://www.gisaid.org), and patient data is being deposited into dbGAP (accession pending).

**Materials and Methods**
*Sample Collection and Processing*
Patient specimens were collected with patients' consent at New York Presbyterian Hospital-Weill Cornell Medical Center (NYPH-WCMC) and then processed for qRT-PCR. Nasopharyngeal (NP) swab specimens were collected using the BD Universal Viral Transport Media system (Becton, Dickinson and Company, Franklin Lakes, NJ) from symptomatic patients.

*Extraction of Viral RNA and qRT-PCR detection*

599 Total viral RNA was extracted from deactivated samples using automated nucleic acid extraction
600 on the QIAsymphony and the DSP Virus/Pathogen Mini Kit (QIAGEN). One step reverse
601 transcription to cDNA and real-time PCR (RT-PCR) amplification of viral targets, E (envelope)
602 and S (spike) genes and internal control, was performed using the Rotor-Gene Q thermocyler
603 (QIAGEN).
604
605 *Twist Synthetic RNAs*
606 We used two fully synthetic RNAs made by in vitro transcription (IVT) from Twist Biosciences,
607 which were synthesized in 5kb pieces with full viral genome coverage of SARS-CoV-2. They
608 were sequence verified to ensure >99.9% viral genome coverage, and come as 1,000,000 copies
609 per µL, 100µL per tube. The two controls are from Wuhan, China (MN908947.3) and
610 Melbourne, Australia (MT007544.1). Reference sequence designs came from NCBI:
611 https://www.ncbi.nlm.nih.gov/nuccore/MT007544 and
612 https://www.ncbi.nlm.nih.gov/nuccore/MN908947.3.
613
614 *Reverse Transcriptase, quantitative real-time PCR (RT-PCR)*
615 Clinical samples were extracted as described above and then tested with qRT-PCR using primers
616 for the E (envelope) gene, which detects all members of the lineage B of the beta-CoVs,
617 including all SARS, SARS-like, and SARS-related viruses, and a second primer set for the S
618 (spike) gene, which specifically detects the SARS-CoV-2 virus. The reaction also contains an
619 internal control that served as an extraction control and a control for PCR inhibition.
620
621 Samples were annotated using qRT-PCR cycle threshold (Ct) value for SARS-CoV-2 primers.
622 Subjects with Ct less than or equal to 18 were assigned "high viral load" label, Ct between 18
623 and 24 were assigned "medium viral load" and Ct between 24 and 40 were assigned "low viral
624 load" classes, with anything above Ct of 40 was classified as negative. We also predicted a
625 combined viral load score using Ct, GloMax QuantiFluor readout from LAMP experiments and
626 fraction of SARS-CoV-2 matching NGS reads in a sample. For this score (40-Ct), (LAMP
627 readout) and (log10(SARS-CoV-2 fraction + 1e-6)) were all normalized between zero and one
628 individually, and summed together using a combination weight of 5 for Ct, 3 for LAMP and 2
629 for NGS.
630
631 *LAMP Primer Sequences*
632 Primers were designed using PrimerExplorer (v4.0), as per guidelines in Zhang *et al*., 2020. This
633 specifically utilized the LAMP-compatible primers for the on the COVID-19 reference genome
634 (NCBI). LAMP's inherent specificity (using 4-6 primers vs. 2 for PCR amplification) in
635 combination with this *in-silico* analysis revealed there is limited opportunity for cross-reactivity
636 to allow for false-positive reporting or affect performance of the N-gene primers for SARS-CoV-
637 2 detection (**Supp Table 5**). Overall, the primers had less than 80% homology with the vast
638 majority of tested pathogen sequences. For any organisms where a primer hit >80% homology,
639 only one of the primers (forward or reverse) had significant homology making an amplified
640 product extremely unlikely. Overall, the results of this analysis predict no significant cross-
641 reactivity or microbial interference. We also assessed the potential impact of sequence variation
642 in circulating strains that might lead to poor amplification. In the thousands of sequences
643 deposited in GISAID (Shu and McCauley, 2017), only one site in the priming region was
644 observed to be polymorphic. The polymorphism (T30359C) was only observed in 106 of 6753

(<2%) sequences with coverage of this region. This variant overlaps the priming site of the LB primer but is not near a 3-prime end and is not anticipated to cause amplification failure. The data from Figure 1 show the use of a single-tube, dual-primer protocol, wherein both the N2 gene and E gene primers are present.

**Primer Sequences: rActin (5′-3′)**

| | |
|---|---|
| ACTB-F3 | AGTACCCCATCGAGCACG |
| ACTB-B3 | AGCCTGGATAGCAACGTACA |
| ACTB-FIP | GAGCCACACGCAGCTCATTGTATCACCAACTGGGACGACA |
| ACTB-BIP | CTGAACCCCAAGGCCAACCGGCTGGGGTGTTGAAGGTC |
| ACTB-LoopF | TGTGGTGCCAGATTTTCTCCA |
| ACTB-LoopB | CGAGAAGATGACCCAGATCATGT |

**Gene E Primer Set (5’-3’)**

| | |
|---|---|
| E1-F3 | TGAGTACGAACTTATGTACTCAT |
| E1-B3 | TTCAGATTTTTAACACGAGAGT |
| E1-FIP | ACCACGAAAGCAAGAAAAAGAAGTTCGTTTCGGAAGAGACAG |
| E1-BIP | TTGCTAGTTACACTAGCCATCCTTAGGTTTTACAAGACTCACGT |
| E1-LB | GCGCTTCGATTGTGTGCGT |
| E1-LF | CGCTATTAACTATTAACG |

**Gene N2 Primer Set (5’-3’)**

| | |
|---|---|
| N2-F3 | ACCAGGAACTAATCAGACAAG |
| N2-B3 | GACTTGATCTTTGAAATTTGGATCT |
| N2-FIP | TTCCGAAGAACGCTGAAGCGGAACTGATTACAAACATTGGCC |
| N2-BIP | CGCATTGGCATGGAAGTCACAATTTGATGGCACCTGTGTA |
| N2-LF | GGGGGCAAATTGTGCAATTTG |
| N2-LB | CTTCGGGAACGTGGTTGACC |

*The LAMP Reaction Setup*

For each well or Eppendorf tube, we utilized a set of six primers (above) for Gene N, the M1800 LAMP Master Mix (NEB), water, and 11.5µL of the sample. The protocol is as follows:

1. Reagents added:
    a. 12.5 µL M1800 LAMP mix (NEB)
    b. 1-5 µL LAMP primers (Gene N or N2/E mix)
    c. 1-11.5 µL of sample
    d. Remaining volume (to 25 µl) $H_2O$
2. Vortex, spin down;
3. Place on Thermocycler at 65ºC for 30 minutes with lid at 105 ºC;
4. Remove tubes, place on ice for 5 seconds;
5. Visualize over lab bench/ice/paper.

*Oropharyngeal Lysate LAMP Run*

Nasopharyngeal and/or oropharyngeal swab samples from 201 patients were collected using a dry cotton swab (cliniswab DS, Aptaca Spa (Italy), #2170/SG/CS). Crude extraction was

691 performed according to pending unpublished European patent [No. 20168 593.0]. In summary,
692 the dry swab was transferred to a 15 ml falcon (Greiner Bio-one, #188.271), filled with 0.5 ml
693 saline solution, and shaken vigorously for 30 min. Afterwards the liquid is transferred to a screw-
694 cap (Sarstedt, #72.692.005). 10µl of the crude RNA extract was added to 12.5 µl 2x NEB LAMP
695 master mix (#M1800L), 2.5 µl of water, 1 µl 25x primer master mix Gen N, and was incubated
696 at 65 °C for 30-40 min. A sample of a patient whom tested positive using an approved qRT-PCR
697 test (sample #1123) was used as an internal control. The read-out was performed visually by
698 color change from pink to yellow or orange.
699
700 The RNA isolation was performed with 50 µl of the crude extract on the QIAsymphony with the
701 DSP Virus/Pathogen Kit (Qiagen, #937055). The RT-PCR was performed using 5 µl of 85 µl
702 eluate with TIB MolBiol Lightmix® MODULAR SARS AND WUHAN CoV E-Gene Kit.
703 Analysis was done with the LightCycler(R) 480 II software and calculated CP values were used
704 for statics and graphical analysis. The Standard curve with a synthetic RNA control (Twist
705 Bioscience, #MT007544.1) was generated using the lamp assay and in parallel with the qRT-
706 PCR. The control RNA was diluted serially 10-fold with water and the absolute copy number,
707 ranging from $10^5$ to $10^{-5}$ was analyzed. Gel electrophoresis after visual read-out of the LAMP
708 assay was done by loading 5 µl of the lamp reaction with 5 µl 2x loading dye on a 1.5 % agarose
709 (Seakem LE Agarose, Lonza #50004) together with 5 µl of a 1kB DNA Ladder (Roche). The
710 electrophoresis was performed at 90 V constant.
711
712 The photometric read-out of the standard curve was performed in a plate reader. To this end the
713 lamp reaction was transferred into a 96-well V-shaped cell-culture plate (Greiner Bio-One,
714 #651180). After measuring the absorbances at 432nm and 560nm, the ratio abs(432)/abs(560)
715 was calculated. The relative absorbance abs(432)/abs(560) was calculated by subtraction of the
716 negative (water) control from all samples (including the negative control). All values above a
717 threshold of 0.1 are considered as a positive assay read-out and are marked with "+", all other
718 values are negative and are marked "-". Statistical and graphical analysis were performed with
719 GraphPad Prism 8.0.4.
720
721 *Light Intensity and Data Processing*
722 Completed reactions were analyzed with the Promega GloMax Explorer (Promega GM3500)
723 fluorometer using the QuantiFluor ONE dsDNA system (Promega E4871). This system recorded
724 fluorometric readout from each well using an emission filter of 500-550nm, an excitation filter
725 set at blue 475 nm, and a high sensitivity setting on the Glomax software. Values were then
726 tabulated and compared with controls (positive and negative). The intensity threshold of 2.5x
727 negative control was used as the threshold for positive detection.
728
729 *DNAse treatment, rRNA depletion, and RNAseq library construction*
730 For library preparation, all samples' total nucleic acid (TNA) were treated with DNAse 1(Zymo
731 Research, Catalog # E1010), which cuts both double-stranded and single-stranded DNA. Post-
732 DNAse digested samples were then put into the NEBNext rRNA depletion v2
733 (Human/Mouse/Rat), Ultra II Directional RNA (10ng), and Unique Dual Index Primer Pairs
734 were used following the vendor protocols from New England Biolabs (except for the first
735 flowcell, see supplemental figures). Kits were supplied from a single manufacturer lot.
736 Completed libraries were quantified by Qubit or equivalent and run on a Bioanalyzer or

equivalent for size determination. Libraries were pooled and sent to the WCM Genomics Core or HudsonAlpha for final quantification by Qubit fluorometer (ThermoFisher Scientific), TapeStation 2200 (Agilent), and QRT-PCR using the Kapa Biosystems Illumina library quantification kit.

*Taxonomic Classification of Sequence Data*

All complete genome or chromosome level assemblies from RefSeq database for archaea, bacteria, protozoa, fungi, human and viruses including SARS-CoV and SARS-CoV-2 genomes were downloaded and used for building a classification database for Kraken2 (k=35, ℓ=31) (O'Leary *et al.,* 2016; Wood *et al.,* 2019).

To get an approximation for the positive and negative classification rate, the BBMap random-reads script was used to simulate 10 million 150bp paired-end Illumina reads from the database sequences (Segata *et al.,* 2016). For the negative test all sequences in the database excluding SARS-CoV and SARS-CoV-2 genome were removed from the sequences and the simulated reads were mapped with the Kraken2 database (Supp Table 1).

For the positive test, the same process was repeated using only SARS-CoV-2 genome (**Supp. Table 2**). Positive results show >99% of SARS-CoV-2 reads uniquely map to either SARS-CoV or SARS-CoV-2, with the remaining 1% are ambiguous, potentially matching multiple taxa (**Supp. Table 2**). All sequences were classified using the Kraken2 database. To remove the potential contamination of reads that are homologous across multiple species we used Kraken2 outputs to filter sequences to either human (uniquely matching Homo sapiens and no other taxon in our database), SARS-CoV-2 (either matching SARS-CoV or SARS-CoV-2 due to homology between these two viruses), and remaining reads that may be coming from unclassified, archaeal, bacterial, viral, fungal, protozoan or ambiguously mapping reads to human or SARS-CoV (*Li*, 2015).

Using kraken2 classifications common respiratory pathogens were identified in clinical samples. Any SARS-CoV-2 negative sample with >0.01% relative abundance (normalized after the exclusion of any human, SARS-CoV-2 and uncharacterized reads) for presence of viral pathogens were classified as potential unrelated viral infection (**Supp. Figure 7**). These samples were used as controls during specific differential expression comparisons to compare the common effects of viral infections on host cells from SARS-CoV-2 infection.

*Viral Genome Assembly*

Reads unambiguously mapping to SARS-CoV or SARS-CoV-2 were aligned to the Wuhan-Hu-1 (Genbank accession MN908947.3) reference using bwa mem (Li, 2013). Variants were called using iVar, and pileups and consensus sequences were generated using samtools (Li *et al.,* 2009; Grubaugh *et al.,* 2019; Greenfield *et al.,* 2020). Any sample with >99% coverage above 10x depth for SARS-CoV-2 genome were taken as reliable samples, which resulted in 155 samples (146 positive, 9 negative). 155 clinical samples were compared to 7,797 SARS-CoV-2 sequences from GISAID (as of April 23, 2020) (9, 10). All sequence filtering, alignments, phylogenetic inference, temporal ordering of sequences and geographic reconstruction of likely transmission events were done using Nextstrain (Katoh and Standley, 2013; Sagulenko *et al.,* 2018; Hadfield *et al.,* 2018). Sequence identity and coverage metrics were calculated using Mview (Brown *et*

783 *al.,* 1998). Phylogenetic trees were created using Nextstrain's augur as described above, and
784 visualized using the ggtree package in R (Yu, 2020).
785
786 *Viral variant calling and allelic fraction estimation*
787 Full-length viral consensus sequences were aligned to the Wuhan-Hu-1 reference using bwa
788 mem (Li, 2013) with default settings. Variants were identified by enumerating the coordinates
789 and query / reference subsequences associated with mismatches (SNV) and gaps in the query
790 (deletion) and reference (insertions) using R/Bioconductor (GenomicRanges, Rsamtools,
791 Biostrings packages) and Imielinski lab gChain packages (https://github.com/mskilab/gChain).
792 Exhaustive variant calling on read alignments was additionally performed using bcftools mpileup
793 and call, with variant read support (VAF, alternate allele count) enumerated with the
794 R/Bioconductor Rsamtools package.
795
796 For each variant, a posterior distribution of variant allele fraction (VAF) was computed using a
797 beta distribution with shape parameters $\theta$ comprising reference and alternate allele counts and
798 pseudo count of 0.5. Variants were classified as het (heterogenous) if $P(VAF > 0.05 \wedge VAF <$
799 $0.95 \mid \theta) > 0.95$. For a given specimen, posterior VAF distributions of $k$ heterogenous variants
800 were then integrated using a histogram density estimator by summing the posterior VAF density
801 across all variants at each point of a grid of 100 points evenly spaced in the (0,1) line. This
802 (unnormalized) mixture density was visualized alongside the individual VAF densities as an
803 estimate of the probability density of a putative viral subclone.
804
805 *SARS-CoV-2 genome wide association study*
806 Population reference and alternate allele counts were computed for all SNV and indel variant
807 calls detected in at least three cases in the A2 clade subset of our NYPH-WCMC sequences (123
808 cases, see above). Similar counts were computed across 537 New York and 7269 non-New York
809 sequences that were obtained from GISAID and incorporated into the Nextstrain tree (see
810 above). A one-tailed Fisher's Exact test was used to compare allele counts in NYPH-WCMC vs.
811 non-New York GISAID cases. All variants with FDR < 0.1 were reported as significant.
812 Significant variants from the initial analysis were replicated in a similar comparison of New
813 York vs non-New York GISAID sequences.
814
815 *Cell Deconvolution Analysis*
816 Bulk RNAseq count data was deconvoluted into cell composition matrices using the MUSIC
817 algorithm (Wang *et al.*, 2019) on a reference single cell RNAseq data from upper respiratory
818 epithelium obtained from nasal brushes and upper airway and lung cells ((Vieira *et al.*, 2019;
819 Lukassen *et al.* 2020).
820
821 *Human Transcriptome Analysis*
822 The reads that mapped unambiguously to the human reference genome via Kraken2 were used to
823 detect the host transcriptional response to the virus. Reads matching *Homo sapiens* were trimmed
824 with TrimGalore, aligned with STAR (v2.6.1d) to the human reference build GRCh38 and the
825 GENCODE v33 transcriptome reference, gene expression was quantified using featureCounts,
826 stringTie and salmon using the nf-core RNAseq pipeline (Pertea *et al.,* 2015; Malinen *et al.,*
827 2005; Johnson *et al.,* 2007; Robinson *et al.,* 2010; Naccache *et al.,* 2014; Zamani *et al.,* 2017;
828 Ewels *et al.,* 2019). Sample QC was reported using fastqc, RSeQC, qualimap, dupradar, Preseq

829 and MultiQC (Okonechnikov *et al.,* 2016; Andrews, 2015; Ewesl *et al.,* 2016; Sayols *et al.,*
830 2016; Wang *et al.,* 2012). Samples that had more than 10 million human mapped reads were
831 used for differential expression analysis. Reads, as reported by featureCounts, were normalized
832 using variance-stabilizing transform (vst) in DESeq2 package in R for visualization purposes in
833 log-scale (Love *et al.,* 2014). Limma voom and DESeq2 were used to call differential expression
834 with either Positive cases vs Negative, or viral load (High/Medium/Low/None excluding any
835 samples with evidence of other viral infections) as reported by either qRT-PCR cycle threshold
836 (Ct) values, or using the inverted normalized Ct value as continuous response for viral levels,
837 where Ct of 15 is 1.0 and Ct of >40 is taken as 0 (Law *et al.,* 2014). Genes with BH-adjusted p-
838 value < 0.01 and absolute log2 fold-change greater than 0.58 (at least 50% change in either
839 direction) were taken as significantly differentially regulated (Benjamini and Hochberg, 1995).
840 The same approaches were repeated correcting for potential confounders in our data in two ways.
841 In the first correction ciliated cell fraction (as predicted by MUSIC) was added as another
842 covariate to our model. For the second correction SVA was run on the data and the resulting two
843 surrogate variables were included in a multivariate model (Leek *et al.,* 2012). The complete gene
844 list for all comparisons are given in Supp Table 3. Resulting gene sets were ranked using log2
845 fold-change values within each comparison and put into GSEA to calculate gene set enrichment
846 for molecular signatures database (MSigDB), MGI Mammalian Phenotypes database and
847 ENCODE transcription factor binding sets (Liberzon *et al.,* 2011; Subramanian *et al.,* 2005;
848 Kuleshov *et al.* 2016; Sergushichev, 2016; Smith *et al.,* 2018). Any signature with adjusted p-
849 value < 0.01 and absolute normalized enrichment score (NES) >= 1.5 were reported (Supp Table
850 3).
851
852 *Cross-reactivity Analysis*
853 Primers were compared with a list of sequences from organism from the same genetic family as
854 SARS-CoV-2 and other high-priority organisms listed in the United States Food and Drug
855 Administration's Emergency Use Authorization Template
856 (https://www.fda.gov/media/135900/download). Using the sequence names in the EUA template,
857 the NCBI taxonomy database was queried to find the highest quality representative sequences for
858 more detailed analysis. Primers were compared to this database using Blast 2.8.1 and the
859 following parameters (word size: 7, match score: 2, mismatch score: -3, gap open cost: 5, gap
860 extend cost: 2). Up to 1000 hits with e-value > 10 were reported.
861
862 *Inclusivity Analysis*
863 Unique, full-length, human-sample sequences were downloaded from the GISAID web interface.
864 These sequences were aligned to NC_045512.2 (Wuhan SARS-CoV-2) using minimap2 -x asm5
865 and visually inspected using IGV 2.8.0 with allele frequency threshold set to 0.01.
866
867 *ACE Inhibitor/Angiotensin Receptor Blocker Cohort Analysis*
868 We compared usage of ACE inhibitors (ACEI) and angiotensin receptor blockers (ARB) in an
869 observational cohort analysis of 8,856 patients with suspected SARS-CoV-2 infection (4,829 of
870 which tested positive). ACEIs and ARBs are commonly taken continuously for several years
871 (Bonarjee et al., 2001). We defined a cohort of ACEI/ARB exposed patients as those that have
872 an ACEI/ARB prescription order sometime after January 1st, 2019. We compared the frequency
873 of ACEI/ARB exposure in three cohort comparisons:
874 i. SARS-CoV-2 tested positive patients versus SARS-CoV-2 tested negative patients,

875 ii. SARS-CoV-2 positive patients who require mechanical ventilation versus those who
876 did not, and
877 iii. SARS-CoV-2 positive patient survival versus death.
878 In addition, we perform one post-hoc comparison to evaluate the individual effects of particular
879 ACEIs or ARBs among SARS-CoV-2 positive patients who are exposed.
880
881 *Cohort and Data Source*
882 Our cohort data for SARS-CoV-2 suspected patients is extracted from the electronic health
883 records at NYPH-CUIMC. We used data collected starting on March 10th, 2020 through April
884 20th, 2020. In addition, we used data from 90,989 patients, who were not tested for SARS-CoV-
885 2 infection and were 18 years or older, with available electronic health records from January 1st,
886 2019 through September 24th, 2019 to represent a comparison population of patients. In both
887 cases, data extracted included disease diagnoses, laboratory measurements, medication and
888 pharmacy orders, and patient demographics. We derived mortality from a death note filed by a
889 resident or primary provider that records the date and time of death. Intubation was used as an
890 intermediary endpoint and is a proxy for a patient requiring mechanical respiration. We used
891 note types that were developed for patients with SARS-CoV-2 infection to record that this
892 procedure was completed. We validated outcome data derived from notes against the patient's
893 medical record using manual review.
894
895 *Experimental Statistical Methods*
896 We conducted univariate analysis of the frequency differences of ACEI/ARB exposure and
897 multivariate regression analysis to account for established risk factors for SARS-CoV-2
898 outcomes (i.e. age, sex, baseline IL-6 upon admission, and comorbidities) (Zhou et al., 2020).
899 We use logistic regression for analysis for comparing cohort (i) and performed survival analysis
900 using a Cox proportional hazards model for cohort comparisons (ii) and (iii). We cannot
901 determine from our data the date of infection. For the study start date for the patient, we use the
902 date of testing positive or the first date a diagnosed patient showed symptoms, whichever came
903 first, minus seven days. Quantitative variables (i.e., age and the first IL-6 measurement) are
904 linearly scaled to [0,1] to facilitate comparison of model coefficients to those of dichotomous
905 variables. Prior to conducting our multivariate analysis, we evaluated and removed correlated
906 covariates. Finally, we repeated the previously described analysis for a cohort restricted to
907 patients with a documented history of clinically diagnosed hypertension. We include all model
908 results in the supplemental tables.
909
910 *Comorbidity Definitions*
911 Risk factors were assigned using OMOP CDM concept IDs 316866 for "Hypertensive Disorder",
912 317576 for "Coronary Arteriosclerosis", 201820 for "Diabetes mellitus", and 437525 for
913 "Overweight". In each case, the concept ID and all descendant concepts were used to define the
914 risk factor phenotype, and individuals were assigned the phenotype if they were assigned any of
915 the codes.
916
917 *Statistical and visualization software*
918 All electronic health data analyses were performed in Python 3.7 and all models were fit using R
919 3.6.3. Survival analyses (Cox regressions and survival curves) were performed with the survival
920 package for R, version 3.1-12. Additional statistical analyses, processing, transformation, and

visualization of genomic data were completed in R / Bioconductor ('Rsamtools', 'GenomicRanges', 'Biostrings') and additional Imielinski Lab R packages ('gTrack', 'gChain', 'gUtils', 'RSeqLib') available at https://github.com/mskilab. Visualization of phylogenies was completed using Auspice and the 'ggtree' and 'ape' libraries for R.

**References**


Agata J, Ura N, Yoshida H, Shinshi Y, Sasaki H, Hyakkoku M, Taniguchi S, Shimamoto K. Olmesartan Is an Angiotensin II Receptor Blocker with an Inhibitory Effect on Angiotensin-Converting Enzyme. *Hypertension Research* 29, 865-874 (2006).

Ajioka RS, Phillips JD, Kushner JP. Biosynthesis of heme in mammals. Biochim Biophys Acta. 2006 Jul;1763(7):723-36

Amanat F, Nguyen T, Chromikova V, Strohmeier S, Stadlbauer D, Javier A, Jiang K, Asthagiri-Arunkumar G, Polanco J, Bermudez-Gonzalez M, Caplivski D, Cheng A, Kedzierska K, Vapalahti O, Hepojoki J, Simon V, Krammer F. A serological assay to detect SARS-CoV-2 seroconversion in humans. *MedRxiv. 2020 Mar 18.* https://www.medrxiv.org/content/10.1101/2020.03.17.20037713v1

Andrews S. FASTQC A Quality Control tool for High Throughput Sequence Data. *Babraham Inst.* (2015).

Benjamini Y, Hochberg Y. Controlling the False Discovery Rate: A Practical and Powerful Approach to Multiple Testing. *J. R. Stat. Soc. Ser. B* (1995)

Broughton JP, Deng X, Yu G, Fasching CL, Singh J, Streithorst J, Granados A, Sotomayor-Gonzalez A, Zorn K, Gopez A, Hsu E, Gu W, Miller S, Pan C, Guevara H, Wadford D, Chen J, Chiu CY. Rapid Detection of 2019 Novel Coronavirus SARS-CoV-2 Using a CRISPR-based DETECTR Lateral Flow Assay. 2020 Mar; 10: 1-27. https://medrxiv.org/cgi/content/short/2020.03.06.20032334v1

Brown, N.P., Leroy C., Sander C. (1998). MView: A Web compatible database search or multiple alignment viewer. *Bioinformatics*. 14 (4):380-381.

Chen X, Schulz-Trieglaff O, Shaw R, Barnes B, Schlesinger F, Källberg M, Cox AJ, Kruglyak S, Saunders CT. Manta: rapid detection of structural variants and indels for germline and cancer sequencing applications, *Bioinformatics*, Volume 32, Issue 8, 15 April 2016, Pages 1220–1222

Chiang C, Layer RM, Faust GG, Lindberg MR, Rose DB, Garrison EP, Marth GT, Quinlan AR, Hall IM. SpeedSeq: Ultra-fast personal genome analysis and interpretation. *Nature Methods* 12(2015): 966–968.

Danko D, Bezdan D, Afshinnekoo E, et al…Mason CE. Global Genetic Cartography of Urban Metagenomes and Anti-Microbrial Resistance https://www.biorxiv.org/content/10.1101/724526v1

Deng X, Achari A, Federman S, Yu G, Somasekar S, et al…Chiu CY. Metagenomic sequencing with spiked primer enrichment for viral diagnostics and genomic surveillance. *Nature Microbiology.* 2020 Mar; 5(3): 443–454.

Dong E, Du H, Gardner L. An interactive web-based dashboard to track COVID-19 in real time. *Lancet Infect Dis.* 2020 Feb 4.

Elbe S, Buckland-Merrett G. Data, disease and diplomacy: GISAID's innovative contribution to global health. *Glob. Challenges* (2017)

Ewels P, Magnusson M, Lundin S, Käller M. MultiQC: Summarize analysis results for multiple tools and samples in a single report. *Bioinformatics* (2016)

Ewels PA et al., nf-core: Community curated bioinformatics pipelines. *Nature* 2020 Feb 13.

Farek J, Hughes D, Mansfield A, Krasheninina O, Nasser W, Sedlazeck FJ, Khan Z, Venner E, Metcalf G, Boerwinkle E, Muzny DM, Gibbs RA, Salerno W. xAtlas: Scalable small variant calling across heterogeneous next-generation sequencing experiments. bioRxiv 295071; doi: https://doi.org/10.1101/295071

Fang L, Karakiulakis G, Roth M. Are patients with hypertension and diabetes mellitus at increased risk for COVID-19 infection? Lancet Respir Med. 2020 Apr;8(4):e21.

Fauver JR, et al., Coast-to-coast spread of SARS-CoV-2 during the early epidemic in the United States. *Cell* 2020.

Gardy J, Loman NJ, Rambaut A. Real-time digital pathogen surveillance - the time is now. Genome Biology. 2015 Jul 30;16(1):155.

Gonzalez-Reiche A, Hernandez MH, Sullivan M, Ciferri B, Alshammary H, Obla A, Fabre S, Kleiner G, Polanco J, Khan Z, Alburquerque B, Guchte A, Dutta J, Francoeur N, Salom B, Oussenko I, Deikus G, Soto J, Sridhar SH, Wang Y, Twyman K, Kasarskis A, Altman DR, Smith M, Sebra R, Aberg J, Krammer F, Garcia-Sarstre A, Luksza M, Patel G, Paniz-Mondolfi A, Gitman M, Sordillo EM, Simon V, Bakel H. Introductions and early spread of SARS-CoV-2 in the New York City area. MedAxiv. 2020. Apr 11. https://www.medrxiv.org/content/10.1101/2020.04.08.20056929v1

Guan WJ, Ni Zy, Hu Y, Liang WH, Ou CQ, He JX, Liu L, Shan H, Lei CL, Hui DSC, Du B, Li LJ, Zeng G, Yuen KY, Chen RC, Tang CL, Wang T, Chen PY, Xiang J, Li SY, Wang JL, Liang ZJ, Peng YX, Wei L, Liu Y, Hu YH, Peng P, Wang JM, Liu JY, Chen Z, Li G, Zheng ZJ, Qiu SQ, Luo J, Ye CJ, Zhu SY, Zhong NS, China Medical Treatment Expert Group for Covid-19. Clinical Characteristics of Coronavirus Disease 2019 in China. *NEJM*. 2020 Feb 28.

Greenfield N, SARS-CoV-2 variant calling and consensus assembly pipeline. GitHub (2020), (available at https://github.com/onecodex/sars-cov-2/).

1013
1014 Grubaugh ND et al., An amplicon-based sequencing framework for accurately measuring
1015 intrahost virus diversity using PrimalSeq and iVar. *Genome Biol*. (2019)
1016
1017 Hadfield J, Megill C, Bell S, Huddleston J, Potter B, Callender C, Sagulenko P, Bedford T, and
1018 Neher RA. 2018. Nextstrain: Real-Time Tracking of Pathogen Evolution. *Bioinformatics* 34
1019 (23): 4121–23.
1020
1021 He F, Deng Y, Li W. Coronavirus Disease 2019 (COVID-19): What we know? J Med Virol.
1022 2020 Mar 14.
1023
1024 Hoffmann M, Weber HK, Schroeder Krüger N, Herrler T, Erichsen S, Schiergens TS, Herrler G,
1025 Wu N, Nitsche A, Müller MA, Drosten C, Pöhlmann S. SARS-CoV-2 Cell Entry Depends on
1026 ACE2 and TMPRSS2 and Is Blocked by a Clinically Proven Protease Inhibitor. Cell. 2020. Mar
1027 5.
1028
1029 Jeffares DC, Jolly C, Hoti M, et al. Transient structural variations have strong effects on
1030 quantitative traits and reproductive isolation in fission yeast. *Nature Communications*. 2017
1031 Jan;8:14061.
1032
1033 Jenkins C and Orsburn B. In silico approach to accelerate the development of mass
1034 spectrometry-based proteomics methods for detection of viral proteins: Application to COVID-
1035 19. 2020 Mar 10. https://www.biorxiv.org/content/10.1101/2020.03.08.980383v1
1036
1037 Johnson WE, Li C, Rabinovic A. Adjusting batch effects in microarray expression data using
1038 empirical Bayes methods. *Biostatistics* (2007).
1039
1040 Katoh K, Standley DM. MAFFT multiple sequence alignment software version 7: Improvements
1041 in performance and usability. *Mol. Biol. Evol.* (2013).
1042
1043
1044 Konrad R, Eberle U, Dangel A, Treis B, Berger A, Bengs K, Fingerle V, Liebl B, Ackermann N,
1045 Sing A. Rapid Establishment of Laboratory Diagnostics for the Novel Coronavirus SARS-CoV-2
1046 in Bavaria, Germany, February 2020. *Eurosurveillance*. 2020 Mar 5.
1047
1048 Kim D, Lee J, Yang J, Kim JW, Kim N, Chang H. The architecture of SARS-CoV-2
1049 transcriptome. *BioRxiv* https://www.biorxiv.org/content/10.1101/2020.03.12.988865v2
1050
1051 Kuleshov, M. V. et al. Enrichr: a comprehensive gene set enrichment analysis web server 2016
1052 update. Nucleic Acids Res. (2016). doi:10.1093/nar/gkw377
1053
1054 Lan L, Xu D, Ye G, Xia C, Wang S, Li Y, Xu H. Positive RT-PCR Test Results in Patients
1055 Recovered from COVID-19. *JAMA* 2020 Feb 27.
1056
1057 Langmead B, and Salzberg S. 2012. Fast Gapped-Read Alignment with Bowtie 2. *Nature*
1058 *Methods* 9 (4): 357–59.

1059
1060 Lauer SA, Grantz KH, Bi Q, Jones FK, Zheng Q, Meredith HR, Azman AS, Reich NG, Lessler J.
1061 The Incubation Period of Coronavirus Disease 2019 (COVID-19) From Publicly Reported
1062 Confirmed Cases: Estimation and Application. *Annals of Internal Medicine*. 2020 Mar 10.
1063 M20-0504.
1064
1065 Law, C. W., Chen, Y., Shi, W. & Smyth, G. K. Voom: Precision weights unlock linear model
1066 analysis tools for RNA-seq read counts. Genome Biol. (2014). doi:10.1186/gb-2014-15-2-r29
1067
1068 Layer RM, Chiang C, Quinlan AR, Hall IM. LUMPY: a probabilistic framework for structural
1069 variant discovery. *Genome Biol.* 2014;15(6):R84.
1070
1071 Leek, J. T., Johnson, W. E., Parker, H. S., Jaffe, A. E. & Storey, J. D. The SVA package for
1072 removing batch effects and other unwanted variation in high-throughput experiments.
1073 Bioinformatics (2012). doi:10.1093/bioinformatics/bts034
1074
1075 Li H. A statistical framework for SNP calling, mutation discovery, association mapping and
1076 population genetical parameter estimation from sequencing data. *Bioinformatics*.
1077 2011;27(21):2987–2993.
1078
1079 Li H, Seqtk: Toolkit for processing sequences in FASTA/Q formats. GitHub (2015).
1080
1081 Li H, Aligning sequence reads, clone sequences and assembly contigs with BWA-MEM. arXiv
1082 Prepr. arXiv (2013), doi:arXiv:1303.3997 [q-bio.GN].
1083
1084 Li H et al., The Sequence Alignment/Map format and SAMtools. *Bioinformatics* (2009).
1085
1086 Li R, Pei S, Chen B, Song Y, Zhang T, Yang W, Shaman J. Substantial undocumented infection
1087 facilitates the rapid dissemination of novel coronavirus (SARS-CoV2). *Science*. 2020 Mar 16.
1088
1089 Liberzon A et al., Molecular signatures database (MSigDB) 3.0. *Bioinformatics* (2011).
1090
1091 Liu R, Han H, Liu F, Lv Z, Wu K, Liu Y, Feng Y, Zhu C. Positive Rate of RT-PCR Detection of
1092 SARS-COV-2 Infection of 4880 Cases from One Hospital in Wuhan, China, from Jan to Feb
1093 2020. *Clinica Chimica Acta* 505 (2020) 172-175.
1094
1095 Lokugamag KG, Hage A, Schindewolf C, Rajsbaum R, Menachery VD. SARS-CoV-2 is
1096 sensitive to type 1 interferon pretreatment. *BioRxiv*
1097 https://www.biorxiv.org/content/10.1101/2020.03.07.982264v3
1098
1099 Love MI et al., Moderated estimation of fold change and dispersion for RNA-seq data with
1100 DESeq2. *Genome Biol.* (2014), doi:10.1186/s13059-014-0550-8.
1101
1102 Lu J et al., Genomic epidemiology of SARS-CoV-2 in Guangdong Province, China. *Cell* 2020
1103

1104 Lukassen, S. et al. SARS-CoV-2 receptor ACE 2 and TMPRSS 2 are primarily expressed in
1105 bronchial transient secretory cells . EMBO J. (2020). doi:10.15252/embj.20105114
1106
1107 Malinen E et al., Analysis of the fecal microbiota of irritable bowel syndrome patients and
1108 healthy controls with real-time PCR. *Am. J. Gastroenterol*. 100, 373–382 (2005).
1109
1110 Metsky HC, Freije CA, Kosoko-Thoroddsen TF, Sabeti PC, Myhrvold C. CRISPR-based
1111 surveillance for COVID-19 using genomically-comprehensive machine learning design. 2020
1112 Mar 2. *BioRxiv*. https://www.biorxiv.org/content/10.1101/2020.02.26.967026v2.
1113
1114 Meyers L, Dien Bard J, Galvin B, Nawrocki J, Niesters HGM, Stellrecht KA, St George K, Daly
1115 JA, Blaschke AJ, Robinson C, Wang H, Cook CV, Hassan F, Dominguez SR, Pretty K,
1116 Naccache S, Olin KE, Althouse BM, Jones JD, Ginocchio CC, Poritz MA, Leber A, Selvarangan
1117 R. Enterovirus D68 Outbreak Detection Through A Syndromic Disease Epidemiology Network.
1118 *J Clin Virol*, 124, 104262, 2020 Mar.
1119
1120 Monteil V, Kwon H, Prado P, Hagelkrüys A, Wimmer RA, Stahl M, Leopoldi A,
1121 Garreta E, Hurtado Del Pozo C, Prosper F, Romero JP, Wirnsberger G, Zhang H,
1122 Slutsky AS, Conder R, Montserrat N, Mirazimi A, Penninger JM. Inhibition of
1123 SARS-CoV-2 Infections in Engineered Human Tissues Using Clinical-Grade Soluble
1124 Human ACE2. *Cell*. 2020 Apr 17.
1125
1126 Naccache SN et al., A cloud-compatible bioinformatics pipeline for ultrarapid pathogen
1127 identification from next-generation sequencing of clinical samples. *Genome Res.* (2014),
1128
1129 Narayanan K, Ramirez SI, Lokugamage KG, Makino S. Coronavirus nonstructural
1130 protein 1: Common and distinct functions in the regulation of host and viral gene
1131 expression. *Virus Res.* 2015 Apr 16;202:89-100.
1132
1133 Okonechnikov K, Conesa A, García-Alcalde F. Qualimap 2: Advanced multi-sample quality
1134 control for high-throughput sequencing data. *Bioinformatics* (2016),
1135
1136 Ong SWX, Tan YK, Chia PY, Lee TH, Ng OT, Wong MSY, Marimuthu K. Air, Surface
1137 Environmental, and Personal Protective Equipment Contamination by Severe Acute Respiratory
1138 Syndrome Coronavirus 2 (SARS-CoV-2) From a Symptomatic Patient. *JAMA*. 2020 Mar 4.
1139
1140 O'Leary NA et al., Reference sequence (RefSeq) database at NCBI: Current status, taxonomic
1141 expansion, and functional annotation. *Nucleic Acids Res*. (2016).
1142
1143 Oudshoorn D, van Boheemen S, Sánchez-Aparicio MT, Rajsbaum R, García-Sastre A, Versteeg
1144 GA. HERC6 is the main E3 ligase for global ISG15 conjugation in mouse cells. PLoS One.
1145 2012;7(1):e29870.
1146
1147 Patel AB, Verma A. COVID-19 and Angiotensin-Converting Enzyme Inhibitors and Angiotensin
1148 Receptor Blockers. What is the evidence? *JAMA* 2020 Mar 24.
1149

1150 Peci A, Winter AL, King EC, Blair J, Gubbay JB. Performance of rapid influenza diagnostic
1151 testing in outbreak settings. J Clin Microbiol. 2014 Dec;52(12):4309-17.
1152
1153 Pertea M et al., StringTie enables improved reconstruction of a transcriptome from RNA-seq
1154 reads. *Nat. Biotechnol*. (2015)
1155
1156 Quilty B, Clifford S, Flasche S, Eggo RM. Effectiveness of airport screening at detecting
1157 travellers infected with 2019-nCoV. 2020. Feb 02. *MedRxiv*.
1158 https://www.medrxiv.org/content/10.1101/2020.01.31.20019265v1
1159
1160 Robinson MD, Oshlack A, A scaling normalization method for differential expression analysis of
1161 RNA-seq data. *Genome Biol.* (2010).
1162
1163 Rausch T, Zichner T, Schlattl A, Stütz AM, Benes V, Korbel JO. DELLY: structural variant
1164 discovery by integrated paired-end and split-read analysis. *Bioinformatics*, Volume 28, Issue 18,
1165 15 September 2012, Pages i333–i339.
1166
1167 Robinson, James T., Helga Thorvaldsdóttir, Wendy Winckler, Mitchell Guttman, Eric S. Lander,
1168 Gad Getz, and Jill P. Mesirov. 2011. Integrative Genomics Viewer. *Nature Biotechnology* 29 (1):
1169 24–26.
1170
1171 Rodriguez-Santana J, Burchard EG, Seibold MA. Type 2 and interferon inflammation strongly
1172 regulate SARS-CoV-2 related gene expression in the airway epithelium. Biorxiv. 2020. Apr 10.
1173 https://www.biorxiv.org/content/10.1101/2020.04.09.034454v1
1174
1175 Sagulenko P, Puller V, Neher RA, TreeTime: Maximum-likelihood phylodynamic analysis.
1176 *Virus Evol.* (2018), doi:10.1093/ve/vex042.
1177
1178 Sayols S, Scherzinger D, Klein H. dupRadar: A Bioconductor package for the assessment of
1179 PCR artifacts in RNA-Seq data. *BMC Bioinformatics* (2016), doi:10.1186/s12859-016-1276-2.
1180
1181 Sergushichev A, An algorithm for fast preranked gene set enrichment analysis using cumulative
1182 statistic calculation. bioRxiv (2016), doi:10.1101/060012.
1183
1184 Santarpia JL, Rivera DN, Herrera V, Morwitzer MJ, Creager H, Santarpia GW,
1185 Crown KK, Brett-Major DM, Schnaubelt E, Broadhurst MJ, Lawler JV, Reid SP, Lowe JJ.
1186 Transmission Potential of SARS-CoV-2 in Viral Shedding Observed at the University of
1187 Nebraska Medical Center. 2020. Mar 26. *MedRxiv*.
1188 https://www.medrxiv.org/content/10.1101/2020.03.23.20039446v2
1189
1190 Schmid-Burgk JL Li D, Feldman D, Słabicki1 M, Borrajo J, Strecker J, Cleary1 B, Regev A,
1191 Zhang F. LAMP-Seq: Population-Scale COVID-19 Diagnostics Using a Compressed
1192 Barcode Space. BioRxiv. https://www.biorxiv.org/content/10.1101/2020.04.06.025635v1
1193
1194 Segata N et al., BBMap short-read aligner, and other bioinformatics tools. *Bioinformatics* (2016).
1195

1196 Sajuthi SP, DeFord P, Jackson ND, Montgomery MT, Everman JL, Rios CL, Pruesse E, Nolin
1197 JD, Plender EG, Wechsler ME, Mak A, Eng C, Salazar S, Medina V, Wohlford EM, Huntsman
1198 S, Nickerson D, Germer S, Zody MC, Abecasis G, Kang H, Rice KM, Kumar R, Oh S,
1199
1200 Shu Y, McCauley J. GISAID: Global initiative on sharing all influenza data – from vision to
1201 reality. *Eurosurveillance* (2017).
1202
1203 Siu KL, Yuen KS, Castaño-Rodriguez C, Ye ZW, Yeung ML, Fung SY, Yuan S, Chan CP, Yuen
1204 KY, Enjuanes L, Jin DY. Severe acute respiratory syndrome coronavirus ORF3a protein
1205 activates the NLRP3 inflammasome by promoting TRAF3-dependent ubiquitination of ASC.
1206 The FASEB Journal (2019), doi: 10.1096/fj.201802418R.
1207
1208 Smith CL, Blake JA, Kadin JA, Richardson JE, Bult CJ, Mouse Genome Database (MGD)-2018:
1209 Knowledgebase for the laboratory mouse. *Nucleic Acids Res*. (2018),
1210
1211 Subramanian A et al., Gene set enrichment analysis: A knowledge-based approach for
1212 interpreting genome-wide expression profiles. *Proc. Natl. Acad. Sci.* (2005),
1213
1214 Sungnak W, Huang N, Bécavin C, Berg M, Queen R, et al., SARS-CoV-2 enry factors are highly
1215 expressed in nasal epithelial cells together with innate immune genes. *Nature Medicine* (2020).
1216
1217 Taiaroa G, Rawlinson D, Featherstone L, Pitt M, Caly L, Druce J, Purcell D, Harty L, Tran T,
1218 Roberts J, Catton M, Williamson D, Coin L, Duchene S. Direct RNA sequencing and early
1219 evolution 2 of SARS-CoV-2. 2020 Mar 7. *BioRxiv*.
1220 https://www.biorxiv.org/content/10.1101/2020.03.05.976167v1
1221
1222 Tang X, Wu C, Li X, Song Y, Yao X, Wu X, Duan Y, Zhang H, Wang Y, Qian Z, Cui J, Lu J.
1223 On the origin and continuing evolution of SARS-CoV-2, *National Science Review*. 2020. Mar 3.
1224
1225 Tanner NA, Zhang Y, Evans TC. Visual Detection of Isothermal Nucleic Acid Amplification
1226 Using pH-Sensitive Dyes. *Biotechniques*. 58 (2), 59-68. 2015 Feb 1.
1227
1228 Updegraff BL, Zhou X, Guo Y, Padanad MS, Chen PH, Yang C, Sudderth J, Rodriguez-Tirado
1229 C, Girard L, Minna JD, Mishra P, DeBerardinis RJ, O'Donnell KA. Transmembrane Protease
1230 TMPRSS11B Promotes Lung Cancer Growth by Enhancing Lactate Export and Glycolytic
1231 Metabolism. Cell Rep. 2018 Nov 20;25(8):2223-2233.e6.
1232
1233 van Doremalen N, Bushmaker T, Morris D, Holbrook M, Gamble A, Williamson B, Tamin A,
1234 Harcourt J, Thornburg N, Gerber S, Lloyd-Smith J, de Wit E, Munster V. Aerosol and surface
1235 stability of HCoV-19 (SARS-CoV-2) compared to SARS-CoV-1. 2020. Mar 17. *New England*
1236 *Journal of Medicine*.
1237
1238 Vieira Braga, F. A. et al. A cellular census of human lungs identifies novel cell states in health
1239 and in asthma. Nat. Med. (2019). doi:10.1038/s41591-019-0468-5
1240

1241 Wang L, Wang S, Li W, RSeQC: Quality control of RNA-seq experiments. *Bioinformatics*
1242 (2012)
1243
1244 Wang, X., Park, J., Susztak, K., Zhang, N. R. & Li, M. Bulk tissue cell type deconvolution with
1245 multi-subject single-cell expression reference. Nat. Commun. (2019). doi:10.1038/s41467-018-
1246 08023-x
1247
1248 Woelfel R, Corman VM, Guggemos W, Seilmaier M, Zange S, Müller MA, Niemeyer D, Kelly
1249 TCJ, Vollmar P, Rothe C, Hoelscher M, Bleicker T, Brünink S, Schneider J, Ehmann R,
1250 Zwirglmaier K, Drosten C, Wendtner C. Virological assessment of hospitalized cases of
1251 coronavirus disease 2019 . 2020. Mar 8.
1252 https://www.medrxiv.org/content/10.1101/2020.03.05.20030502v1
1253
1254 Wood DE, Lu J, Langmead B. Improved metagenomic analysis with Kraken 2. *Genome Biol*.
1255 (2019).
1256
1257 Wylie AL, Fournier J, Casanovas-Massana A, Campbell M, Tokuyama M, Vijayakumar P, et al.,
1258 Saliva is more sensitive for SARS-CoV-2 detection in COVID-19 patients than nasopharyngeal
1259 swabs. *MedRxiv*. https://www.medrxiv.org/content/10.1101/2020.04.16.20067835v1
1260
1261 Yu G. Using ggtree to visualize data on tree-like structures. *Current Protocols in Bioinformatics*,
1262 2020, 69:e96. doi: 10.1002/cpbi.96.
1263
1264 Yu L, Wu S, Hao X, Li X, Liu X, Ye S, Han H, Dong X, Li X, Li J, Liu J, Zhang W, Pelechano
1265 V, Chen W, Yin X. Rapid Colorimetric Detection of COVID-19 Coronavirus Using a Reverse
1266 Transcriptional Loop-Mediated Isothermal Amplification (RT-LAMP) Diagnostic Platform:
1267 iLACO. 2020 Feb 24.
1268 https://www.medrxiv.org/content/10.1101/2020.02.20.20025874v1
1269
1270 Zamani S et al., *Mycobacterium avium* subsp. *paratuberculosis* and associated risk factors for
1271 inflammatory bowel disease in Iranian patients. *Gut Pathog*. 9, 1 (2017).
1272
1273 Zhao Z, Sokhansanj BA, Rosen G. Characterizing geographical and temporal dynamics of novel
1274 coronavirus SARS-CoV-2 using informative subytype markers. *BioRxiv*
1275 https://www.biorxiv.org/content/10.1101/2020.04.07.030759v3
1276
1277 Zhang P, Zhu L, Cai J, Lei F, Qin J, et al. Association of Inpatient Use of Angiotensin
1278 Converting Enzyme Inhibitors and Angiotensin II Receptor Blockers with Mortality Among
1279 Patients With Hypertension Hospitalized With COVID-19. *Circulation Research*. 2020 Apr 17.
1280
1281 Zhang Y, Odiwuor N, Xiong J, Sun L, Nyaruaba RO, Wei H, Tanner NA. Rapid Molecular
1282 Detection of SARS-CoV-2 (COVID-19) Virus RNA Using Colorimetric LAMP. 2020. Feb 29.
1283 *MedRxiv* https://www.medrxiv.org/content/10.1101/2020.02.26.20028373v1
1284
1285 Zhou F, Yu T, Du R, Fan G, Liu Y, Liu Z, Xiang J, Wang Y, Song B, Gu X, Guan L, Wei Y, Li
1286 H, Wu X, Xu J, Tu S, Zhang Y, Chen H, Cao B. Clinical course and risk factors for mortality of

1287 adult inpatients with COVID-19 in Wuhan, China: a retrospective cohort study. *Lancet*. 2020
1288 Mar 11.
1289

**Figures and Legends for "Shotgun Transcriptome and Isothermal Profiling of SARS-CoV-2 Infection Reveals Unique Host Responses, Viral Diversification, and Drug Interactions" (Butler *et al.* 2020)**

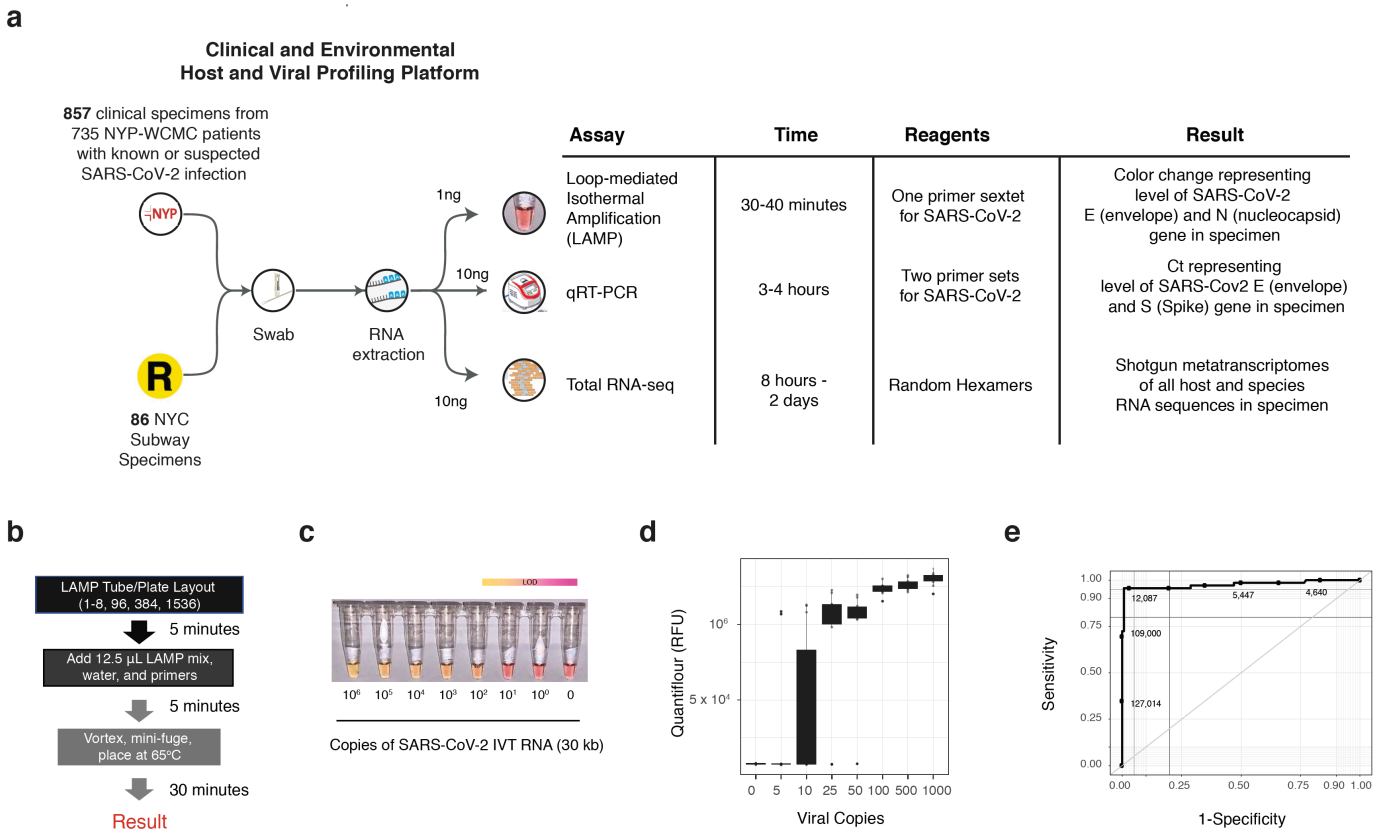


**Figure 1. Sample Processing, the Loop-Mediated Isothermal (LAMP) Reaction and Synthetic RNA Validation.** (a) Clinical and environmental samples collected with nasopharyngeal (NP) and isohelix swabs respectively, were tested with RNA-sequencing, qRT-PCR, and LAMP. (b) The test samples were prepared using an optimized LAMP protocol from NEB, with a reaction time of 30 minutes. (c) Reaction progress was measured for the Twist SARS-CoV-2 synthetic RNA (*MT007544.1*) from 1 million molecules of virus ($10^6$), then titrated down by $\log_{10}$ dilutions. The colorimetric findings of the LAMP assay are based on a yellow to pink gradient with higher copies of SARS-CoV-2 RNA corresponding to a yellow color. The limit of detection (LoD) range is shown with a gradient after 30 minutes between 10 and 100 viral copies (lower right). (d) Replicates of the titrated viral copies using LAMP, as measured by QuantiFluor fluorescence. (e) The sensitivity and specificity of the LAMP assay from 201 patients (132 negative and 69 positive for SARS-CoV-2, as measured by qRT-PCR). Thresholds are DNA quantified by the QuantiFluor.

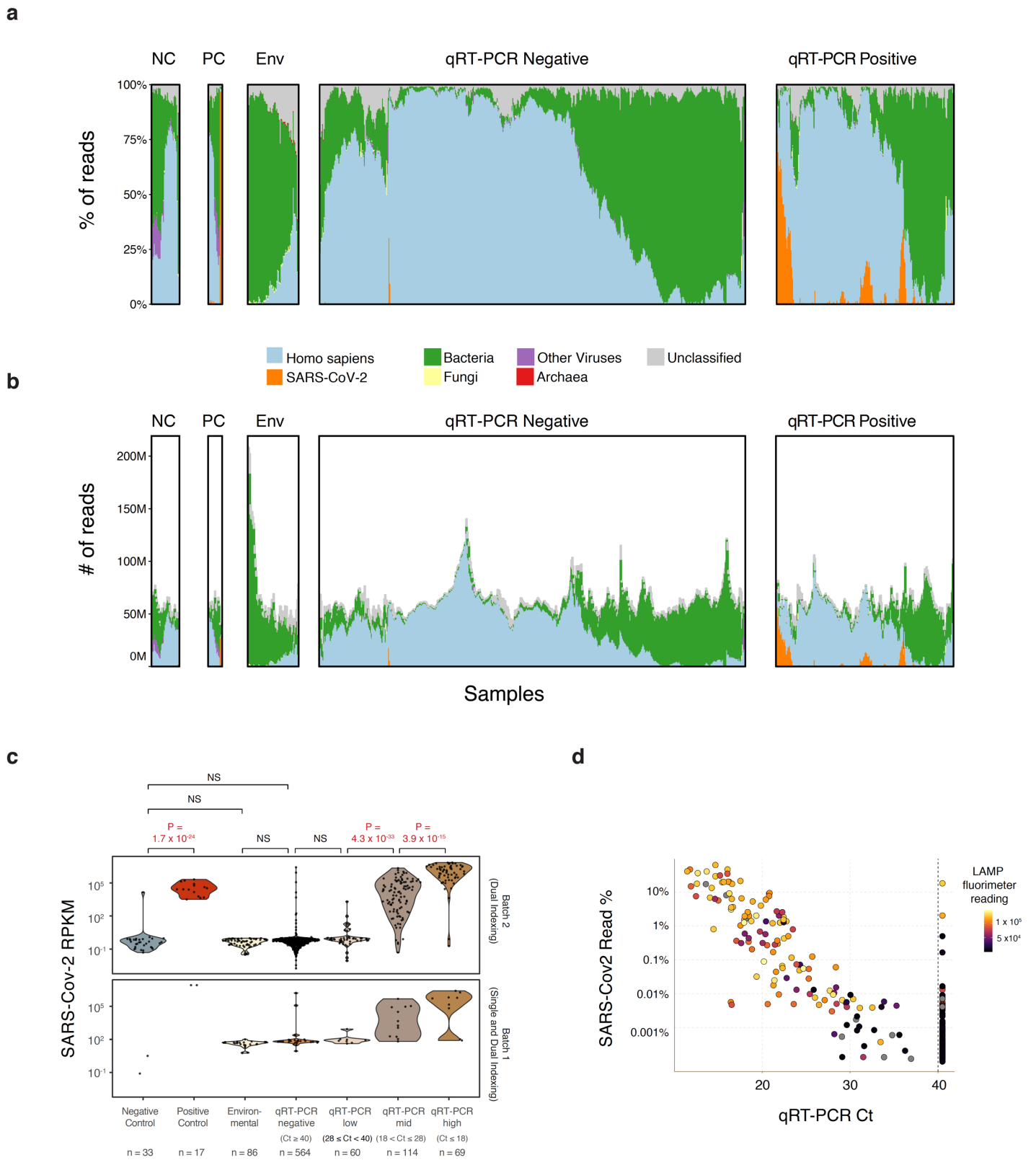


**Figure 2. Full transcriptome profiles of SARS-CoV-2 Patients with NGS, qRT-PCR, and LAMP.** (a,b) Read mapping to archaea (red), bacteria (green), fungi (yellow), human (blue), and SARS-CoV-2 (orange), and other viruses (grey), across the clinical controls (CN, CP), environmental samples, qRT-PCR negative, and qRT-PCR positive samples. (c) Clinical samples tested by qRT-PCR (Positive, n=255, or Negative, n=564) were sequenced and run through the LAMP assay. These results were compared to the buffer blanks (Negative Control, CN, n=33), Vero E6 cell extracts with SARS-CoV-2 infection (Positive Controls, CP, n=17), and Subway Samples (Environmental, Env, n=86). Read proportions are shown on the y-axis. (d) SARS-CoV-2 abundance, as measured with NGS and percentage of reads (y-axis) is compared to the Ct Threshold for qRT-PCR (x-axis), with lower Ct values representing higher viral abundance, and the LAMP reaction output (Fluorimeter values, black to yellow scale).

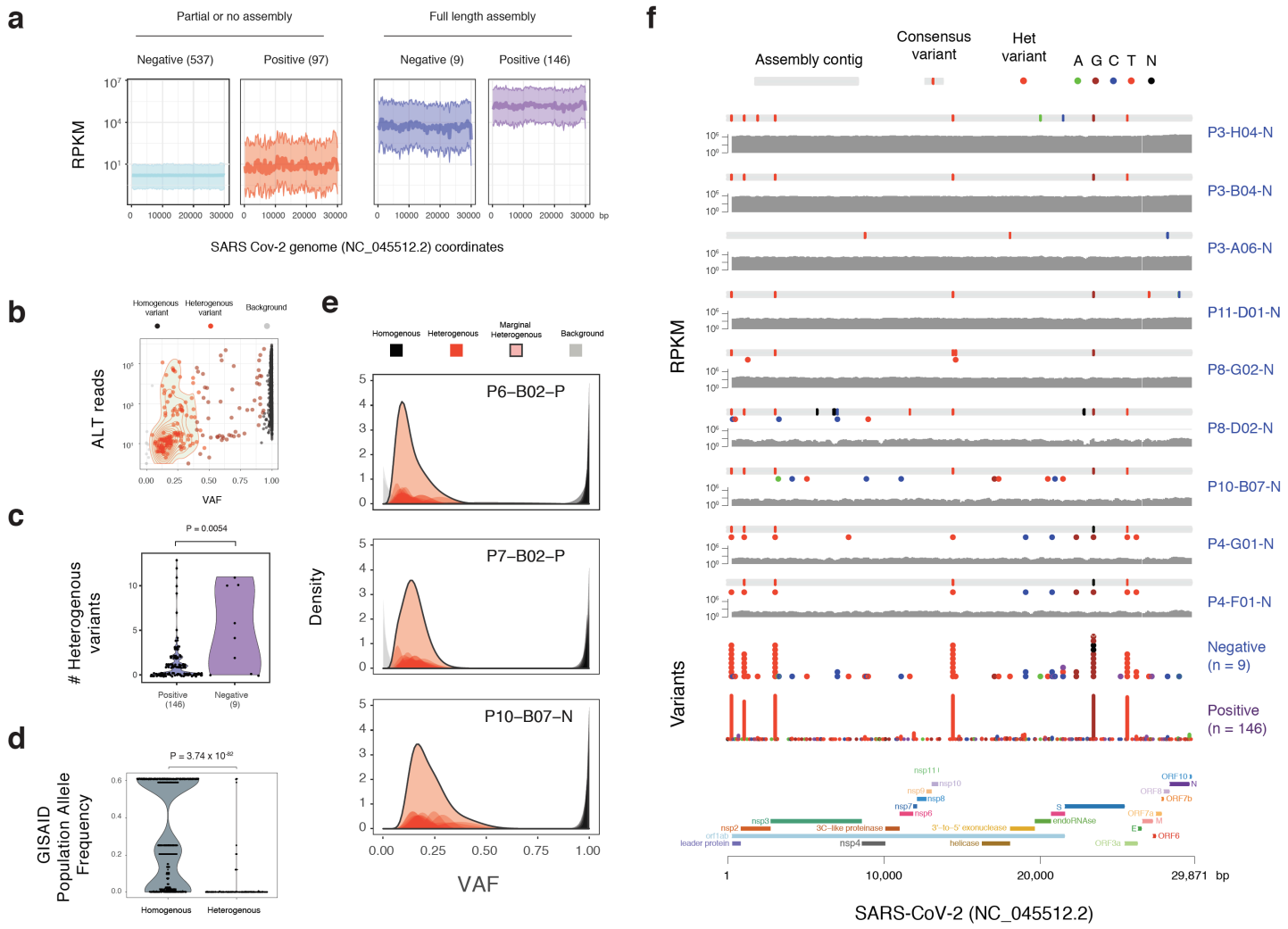


**Figure 3. Viral genome assemblies and variants** (a) Clinical samples tested by qRT-PCR (Negative, N) were compared to RNA-seq coverage (Read per Kilobase per Million Reads, RPKM, y-axis) for the set of fully-assembled positive samples (n=146, 9) vs. those with partial or no assemblies (left, n=537, 97). (b) Variant allele frequencies (VAF, x-axis) for alternative alleles (y-axis) were calculated for all variants across viral strains, with heterogenous (het, 5%<x<95%, red) variants shown as well as homogenous (black) variants with VAF>0.95. (c) Proportion of het variants (y-axis) is shown for those tested by qRT-PCR and shown as negative or positive (x-axis). (d) The frequency of variants present in the GISAID global database of virus sequences (y-axis) is shown for variant types (x-axis). (e) The distribution and density of the VAF for three exemplar samples are shown relative to their variant type (top) (f) The assembled contigs (grey) the consensus variants (red dots) relative to the reference, and coverage (RPKM) are shown for a set of clinical samples, relative to the reference SARS-CoV-2 genome annotation (bottom), gene segments (colored bars), and histogram of variants from qRT-PCR positive and negative samples (variants y-axis).

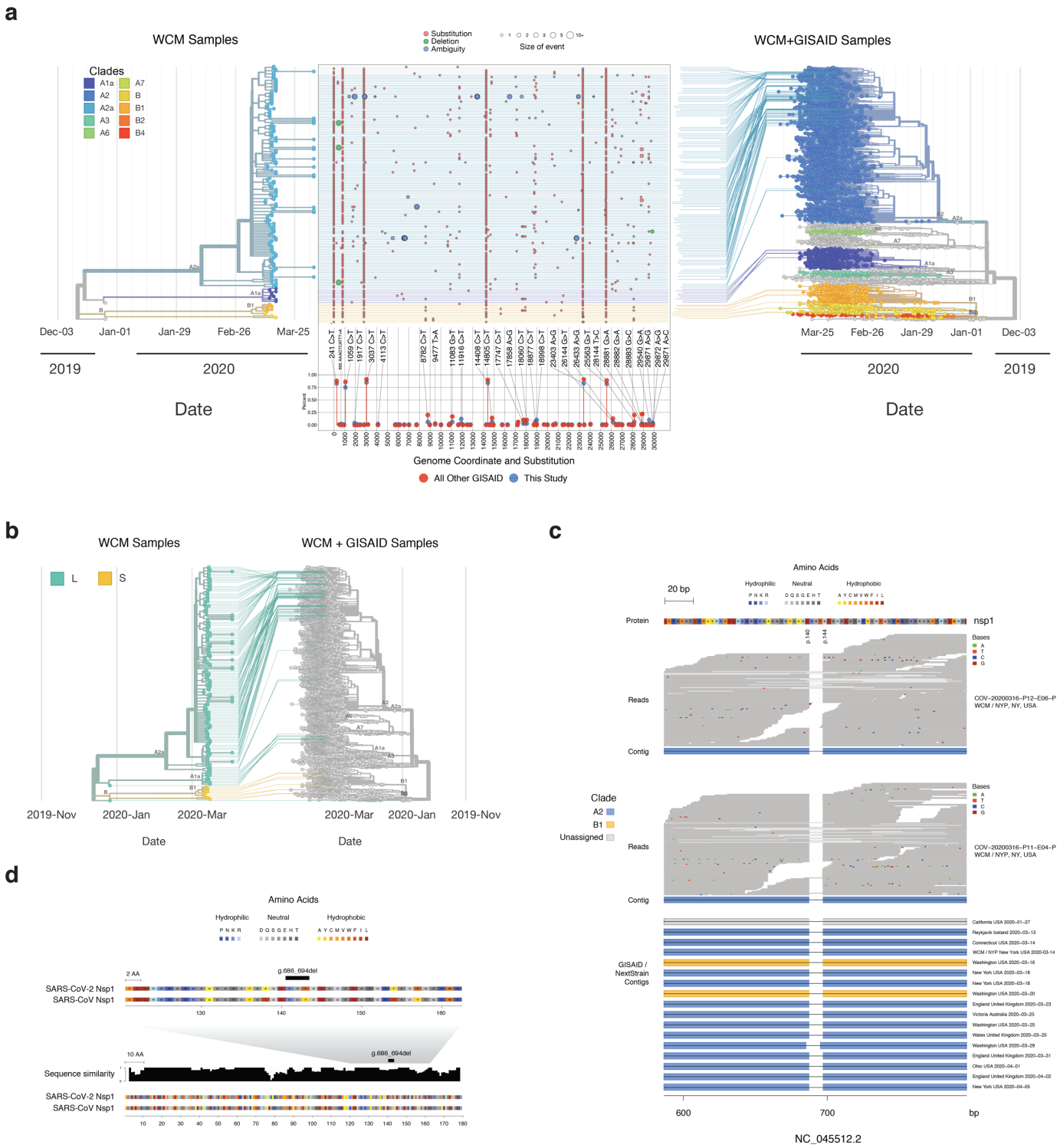


**Figure 4 – The mutational landscape SARS-CoV-2.** (a) The phylogenetic placement of these SARS-CoV-2 samples is shown on the tree (left) and the global map of known SARS-CoV-2 genomes (right). Genetic variants called from the RNA-seq data (middle) show a range of variants that are distinct from the Wuhan reference strain, and the samples from this study, highlighted in blue, show enrichment for European and Asian alleles. The annotation track on the bottom shows variants called in these samples alongside all other GISAID samples. Samples that diverge from GISAID by more than 5% in either direction are annotated, including their coordinate and substitution event. (b) Proportion of the L (green) and S strain (yellow) are shown for the NYC viruses. Phylogeny of samples from this study on the left and total GISAID samples on the right, with a map of variants in this study's samples in the middle, colored by event type and sized by number of nucleotides impacted. Annotation track on the bottom shows frequency of alternate alleles in this study and in the GISAID database. (c) The 9-bp deletion in ORF1b (NSP1 protein) that was detected in samples from three NYPH-WCMC patients was confirmed in the GISAID database (bottom tracks). Read-level support is shown in the top tracks for

two of the variants, with aligned contigs visualized below. Assembly alignments for 17 additional cases harboring this deletion, including 1 additional case from this study are shown in the bottom track. (d) Alignment of SARS-CoV-2 to SARS-CoV NSP1 protein sequence is shown, with an enlarged view showing a sequence similarity track (normalized protein alignment score in 5 amino acid sliding window) and the 9-bp deletion region delineated.

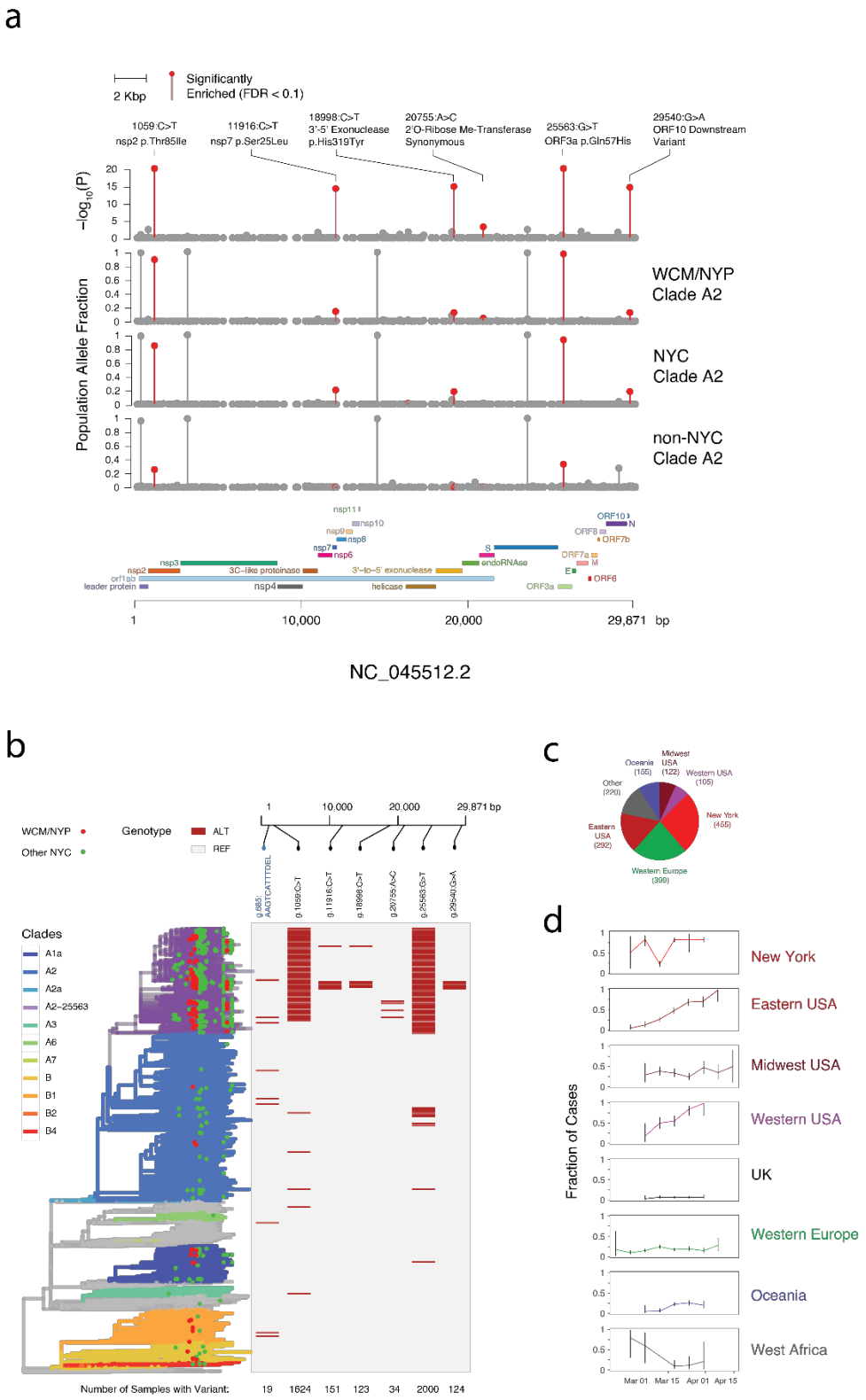


**Figure 5. Variant and Subclade Analysis**. (a) Six variant alleles were found to be significantly enriched by population allelic fraction within this set of 93 WCM/NYP cases as compared with non-NYC strains of Nextstrain clade A2 (1059:C>T P = 2.13 x $10^{-47}$, 11916:C>T P = 6.26 x $10^{-15}$, 18998:C>T P= 1.53 x $10^{-15}$, 20755:A>C P = 6.6 x$10^{-4}$, 25563:G>T P = 7.92 x $10^{-50}$, 29540:G>A P = 2.68 x $10^{-15}$). These variants demonstrated similar PAF enrichment within all other NYC strains as compared to non-NYC clade A2 (1059:C>T P = 3.36 x $10^{-146}$, 11916:C>T P = 3.53 x $10^{-74}$,

18998:C>T P= 3.94x $10^{-73}$, 20755:A>C P = 7.71 x $10^{-3}$, 25563:G>T P = 1.45 x $10^{-154}$, 29540:G>A P = 2.07 x $10^{-72}$). (b) (left) Phylogenetic tree produced by the Nextstrain analysis with clade affiliations and nodes corresponding to WCM/NYP in red and other NYC cases in green. (right) occurrence of the six NYC-enriched alleles and the 9 nucleotide deletion across genomes. (c) Raw counts of cases present within this A2-25563 subclade demonstrated a predominance of European and North American cases, with Western Europe and New York together comprising the majority of strains. (d) Fraction of A2-25563 cases from each region of the world.

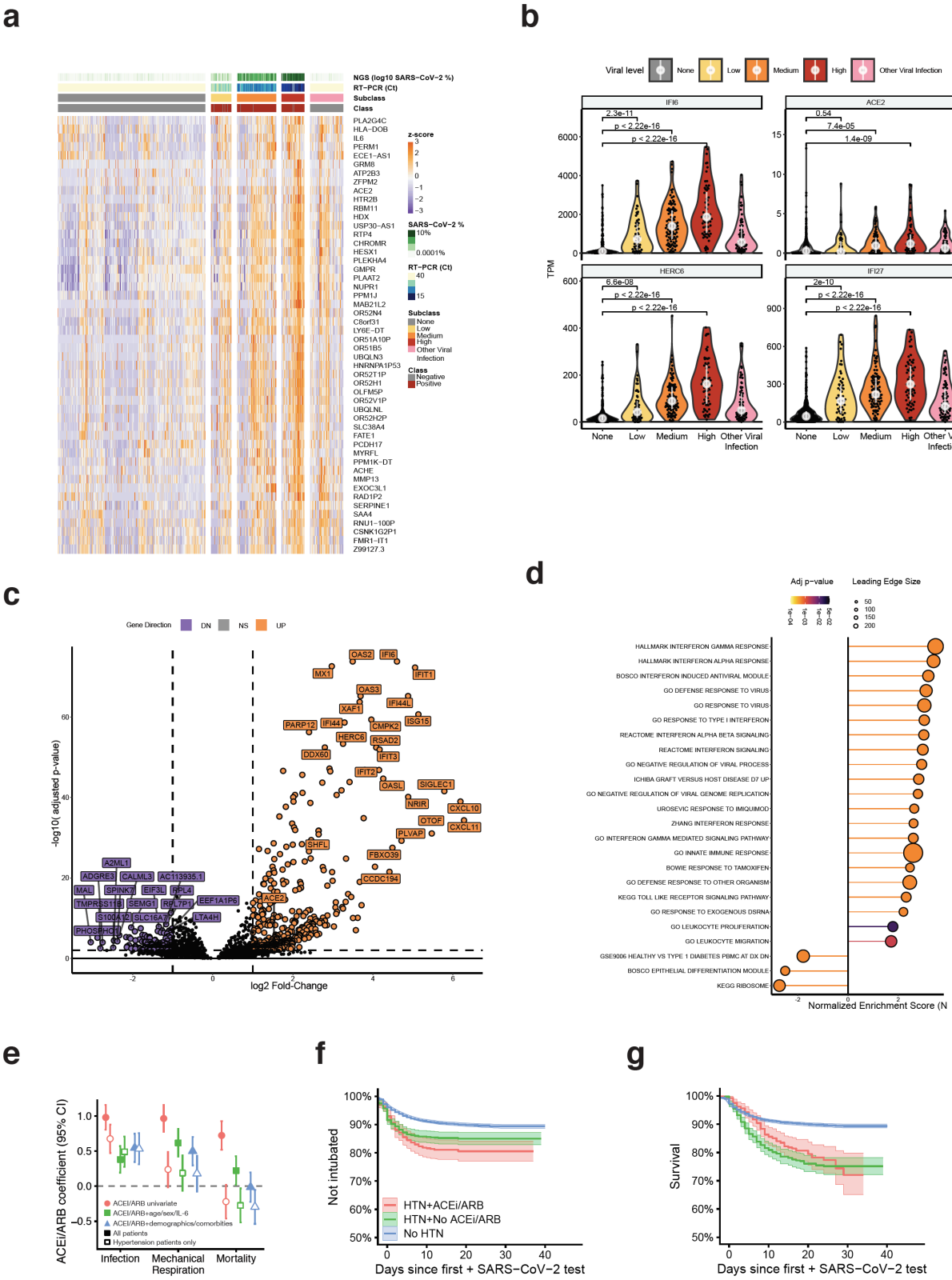

**Figure 6: Host transcriptome responses and risk to SARS-CoV-2.** (top row) Samples were quantified by a range of viral load, including RNA-seq ($log_{10}$ SARS-CoV-2 % of reads), and qRT-PCR (Ct values) to create a three-tier range of viral load for the positive samples (right) compared to the clinically-annotated negative samples (class, red or grey) and those samples with other viral infections that were SARS-CoV-2 negative by qRT-PCR. (b) The differentially expressed genes of qRT-PCR positive patients compared to qRT-PCR patients showed up-regulated (orange) genes as well as down-regulated (purple) genes. (b) Up-regulated genes, with boxplots across all samples, include *IFI6*, *ACE2*, *SHFL*, *HERC6*, *IFI27*, and *IFIT1*, based on data from (c), which is the total set of DEGs. The full set is shown in an intersecting heat map, with a core set of up-regulated genes (orange) distinct form the set of down-regulated genes (purple), compared to genes that are not significantly differently expressed (grey) in any comparison (DESeq2, q-value <0.01, |logFC| >0.58). (d) GSEA enrichment of significant pathways, with color indicating statistical significance and circle size the number of genes on the leading edge (e) Regression coefficients for variables indicating exposure/history of exposure to ACEI/ARBs inhibitors for each of the three cohort comparisons: (left) test outcome in a cohort of patients suspected of SARS-CoV-2 infection, (middle) requirement of mechanical respiration in patients who tested positive, (right) mortality in patients who tested positive. Univariate analyses are shown as red circles. The green triangles coefficients are when correcting for age, sex, and baseline IL-6 levels take upon admission. The blue squares are from a model that includes age, sex, and IL-6 as well as comorbidities including CAD/CHD, diabetes, being overweight, or obesity, and self-reported race and ethnicity. Additionally, open markers indicate the same analyses but restricted to only patients with clinically diagnosed hypertension. (f) Curves for patients requiring mechanical respiration (identified by intubation procedure notes) as a function of drug class (g) and survival, conditioned on hypertension status and ACEI/ARB exposure status.

**Table 1. Baseline characteristics of SARS-CoV-2 suspected cohort.** General population refers to a comparison cohort of individuals administered drugs at NYPH-CUIMC between January 1, 2019 – September 24, 2019 who were not later tested for SARS-COV-2 infection.

| Variable | General | Tested | COV+ | COV+/Intubated | COV+/Died |
|---|---|---|---|---|---|
| N (% of tested) | 90989 | 8856 (100%) | 4829 (54.5%) | 534 (6%) | 528 (6%) |
| ACEI | 2201 (2.4%) | 408 (4.6%) | 310 (6.4%) | 78 (14.6%) | 57 (10.8%) |
| ARB | 2113 (2.3%) | 400 (4.5%) | 295 (6.1%) | 70 (13.1%) | 65 (12.3%) |
| ACEI and ARB | 163 (<0.1%) | 28 (0.3%) | 22 (0.5%) | 7 (1.3%) | 4 (0.8%) |
| Median age (50%) | 34.6 (27.5-42.2) | 57.2 (38.3-71.8) | 62.4 (47.8-75) | 65.4 (54.4-74.8) | 78.2 (69.9-87) |
| Male | 31228 (34.3%) | 4001 (45.2%) | 2546 (52.7%) | 336 (62.9%) | 309 (58.5%) |
| Black/African-American | 1739 (1.9%) | 2047 (23.1%) | 1229 (25.5%) | 125 (23.4%) | 95 (18%) |
| Caucasian | 108 (0.1%) | 2587 (29.2%) | 1249 (25.9%) | 127 (23.8%) | 141 (26.7%) |
| Asian or Pacific Islander | 1564 (1.7%) | 237 (2.7%) | 106 (2.2%) | 4 (0.7%) | 4 (0.8%) |
| Other race | 79 (0.1%) | 2134 (24.1%) | 1250 (25.9%) | 156 (29.2%) | 165 (31.2%) |
| Missing race | 140 (0.2%) | 1851 (20.9%) | 995 (20.6%) | 122 (22.8%) | 123 (23.3%) |
| Hispanic/Latino | 13875 (15.2%) | 2811 (31.7%) | 1704 (35.3%) | 260 (48.7%) | 251 (47.5%) |
| Non-Hispanic/Latino | 23537 (25.9%) | 3576 (40.4%) | 1811 (37.5%) | 151 (28.3%) | 156 (29.5%) |
| Other ethnicity | | 95 (1.1%) | 61 (1.3%) | 7 (1.3%) | 13 (2.5%) |
| Missing ethnicity | 53577 (58.9%) | 2374 (26.8%) | 1253 (25.9%) | 116 (21.7%) | 108 (20.5%) |
| Hypertension | 15298 (16.8%) | 2200 (24.8%) | 1392 (28.8%) | 243 (45.5%) | 310 (58.7%) |
| CAD/CHD | 1978 (2.2%) | 831 (9.4%) | 511 (10.6%) | 92 (17.2%) | 137 (25.9%) |
| Diabetes | 7239 (8.0%) | 1340 (15.1%) | 867 (18%) | 163 (30.5%) | 203 (38.4%) |
| Overweight | 12878 (14.2%) | 923 (10.4%) | 560 (11.6%) | 95 (17.8%) | 101 (19.1%) |
| No RF | 64695 (71.1%) | 6223 (70.3%) | 3212 (66.5%) | 264 (49.4%) | 198 (37.5%) |
| Median IL-6 (50%) | - | 67.8 (29.3-152.9) | 70.2 (30.8-154.4) | 152.8 (72.9-278.1) | 146.1 (81.2-284.8) |

**Table 2. Comparison between ACE/ARB exposure and CCB exposure**. To evaluate if evidence of hypertension treatment is confounding association between ACE/ARB exposure and infection. These analyses were completed using only patients with hypertension. In each test the ACE/ARB groups showed significantly greater rates of infection. CCB exposure was not found to be associated with infection.

| Comparison | OR | 95% CI | p–value |
|---|---|---|---|
| ACEi vs none | 1.481 | 1.121–1.965 | 4.7e–03 |
| ARB vs none | 1.776 | 1.298–2.449 | 2.2e–04 |
| ACEi/ARB vs none | 1.603 | 1.28–2.012 | 2.6e–05 |
| CCB vs none | 1.052 | 0.846–1.308 | 0.67 |
| ACEi vs CCB | 1.408 | 1.034–1.922 | 0.02 |
| ARB vs CCB | 1.688 | 1.201–2.388 | 2.0e–03 |
| ACEi/ARB vs CCB | 1.524 | 1.175–1.98 | 1.1e–03 |
| ACEi vs ¬ACEi | 1.253 | 0.963–1.637 | 0.09 |
| ARB vs ¬ARB | 1.511 | 1.128–2.043 | 4.6e–03 |
| ACEi/ARB vs ¬ACEi/ARB | 1.374 | 1.135–1.668 | 9.0e–04 |
| CCB vs ¬CCB | 0.891 | 0.744–1.068 | 0.2 |

## Supplemental Figures and Tables

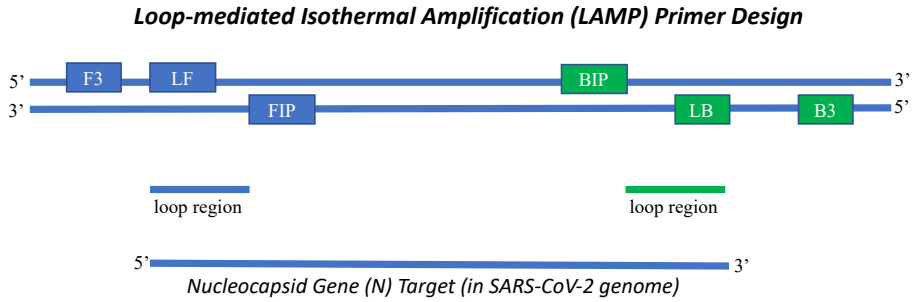


**Supplemental Figure 1. LAMP Primer Design.** PrimerDesigner (v4) was used to create a set of six primers that would specifically target the nucleocapsid gene (N) in the SARS-CoV-2 genome. Primer sequences are listed in the methods section.

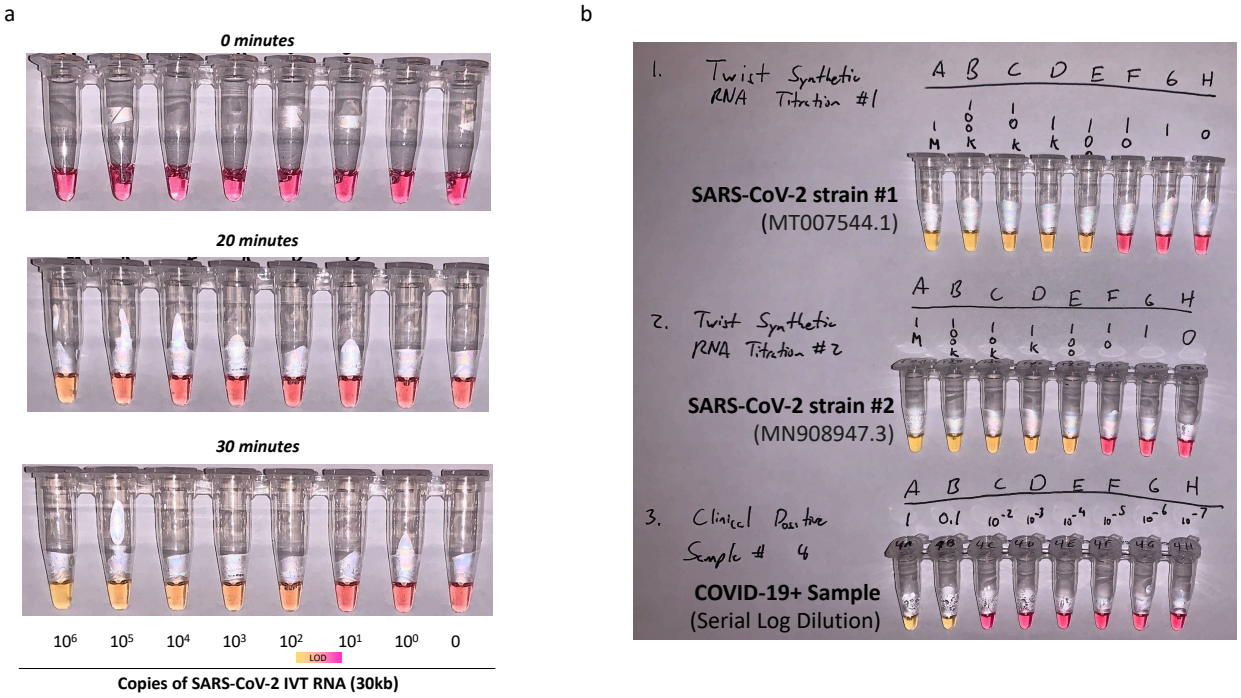


**Supplemental Figure 2. Additional Testing and Titration of the LAMP Assay with Synthetic and Clinical Samples.** Samples were prepared using the LAMP protocol with a reaction time of 30 minutes. Reaction progress was measured (a) from 0, 20, and 30 minutes. (b) This was repeated for both Twist SARS-CoV-2 synthetic RNAs (MT007544.1, top and MN908947.3, middle*)* from 1 million molecules of virus ($10^6$), then titrated down by log10 dilutions. Limit of Detection (LOD) range is shown with a gradient after 30 minutes between 10 and 100 viral copies. (bottom) A clinically positive sample that was not detectible by Qubit (<0.05 ng/mL) was nonetheless detected by LAMP, in accordance with detection of low viral titer samples.

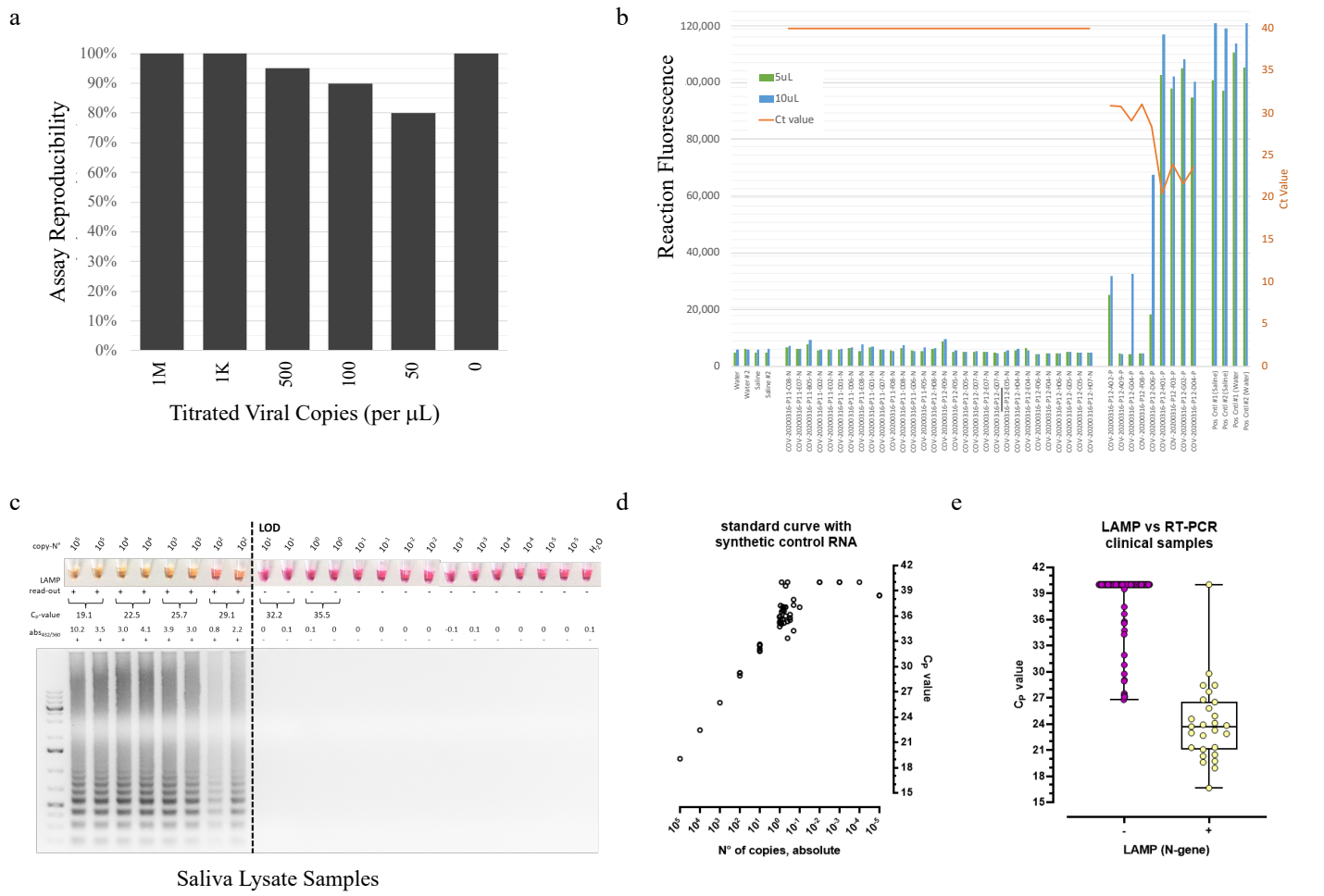


**Supplemental Figure 3. Reproducibility, sensitivity, and specificity for the LAMP Assay.** (a) Testing with a synthetic SARS-CoV-2 RNA that was serially titrated and measured in replicates (n=10) showed 100% and 95% reproducibility at 1,000 and 500 copies, respectively, with lower rates at lower viral titers. (b) Replicates of a clinically positive (by qRT-PCR) sample at 10 uL (blue) compared to 5uL (green) showed high concordance, with greater sensitivity with increased reaction volume. (c) Whole oropharyngeal swab lysates from clinical positive (Cp-value >0) and negative samples (Cp = NA) were used to test the LAMP reaction. (d) The standard curve with synthetic RNA was also tested relative to absolute number of copies (x-axis) and the Cp value (y-axis). (e) The Cp value for the LAMP positive (+, right) and negative (-, left) were compared to the Cp value from qRT-PCR (y-axis).

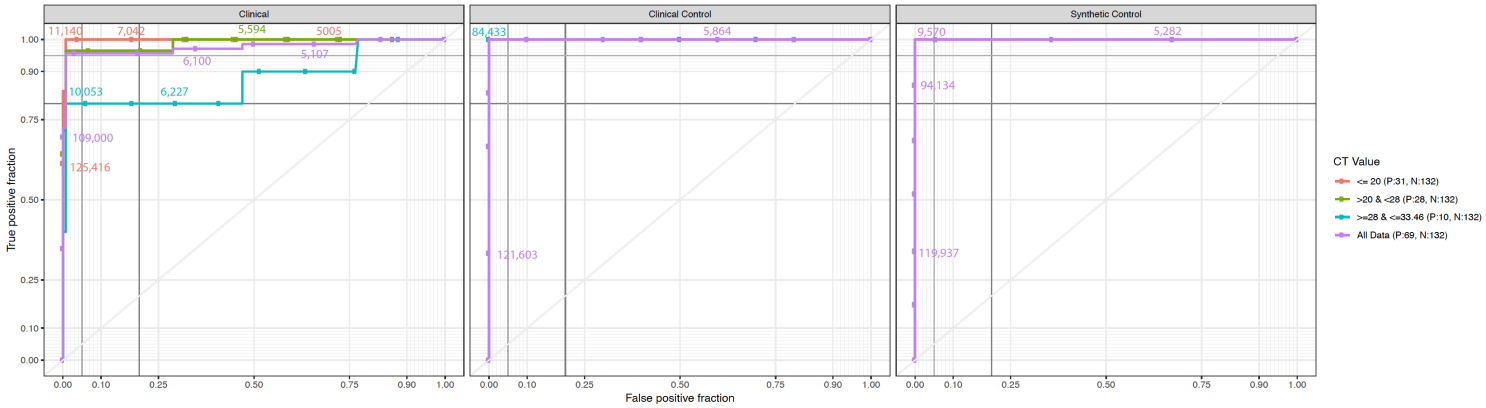


**Supplemental Figure 4. Ct and RFU (Relative Fluorescence Units) Thresholds for the LAMP Assay.** With increasing viral load, as measured by qRT-PCR, the LAMP assay shows an increased sensitivity (y-axis) and specificity (y-axis). For high and medium viral count samples (Ct < 28, red and green line), we see 100% sensitivity, and for low viral count, we see 81% sensitivity and 100% specificity (blue). Across all data (purple), we see 95.6% sensitivity and 99.4% specificity. RFU thresholds are shown as numbers.

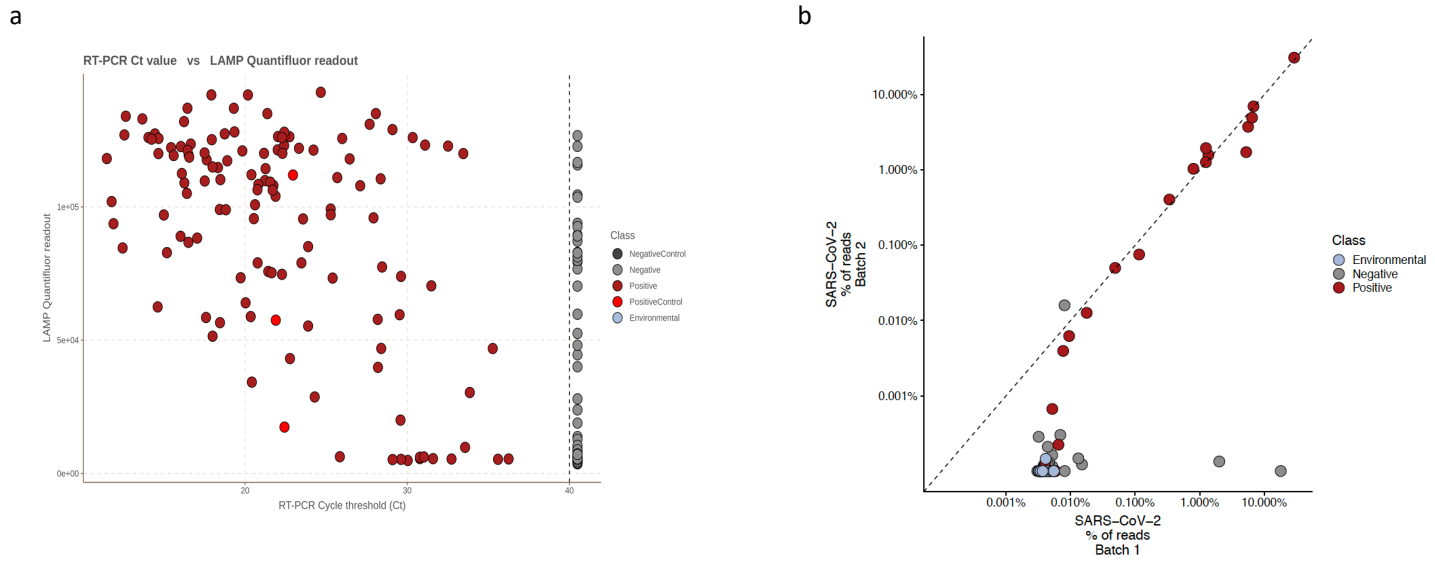


**Supplementary Figure 5. Correlation between LAMP Reaction Output and qRT-PCR as well as RNA-seq replicates.** (a) Clinical samples tested by qRT-PCR (Positive, dark red or Negative, light grey) were run with the LAMP assay and compared to the buffer blanks (Negative Control, dark grey), Synthetic RNAs or Vero 6 cell extracts with SARS-CoV-2 infection (Positive Controls, light red), and Subway Samples (Environmental, blue, lower right). The DNA abundance, as measured with the GloMax QuantiFluor (y-axis) is compared to the Ct Threshold for qRT-PCR (x-axis), with lower Ct values representing higher viral abundance. (b) RNA-seq replicates from batch 1 (single index) vs. batch 2 (dual index adapters), showing the broader dynamic range of dual-index libraries (R=0.85).

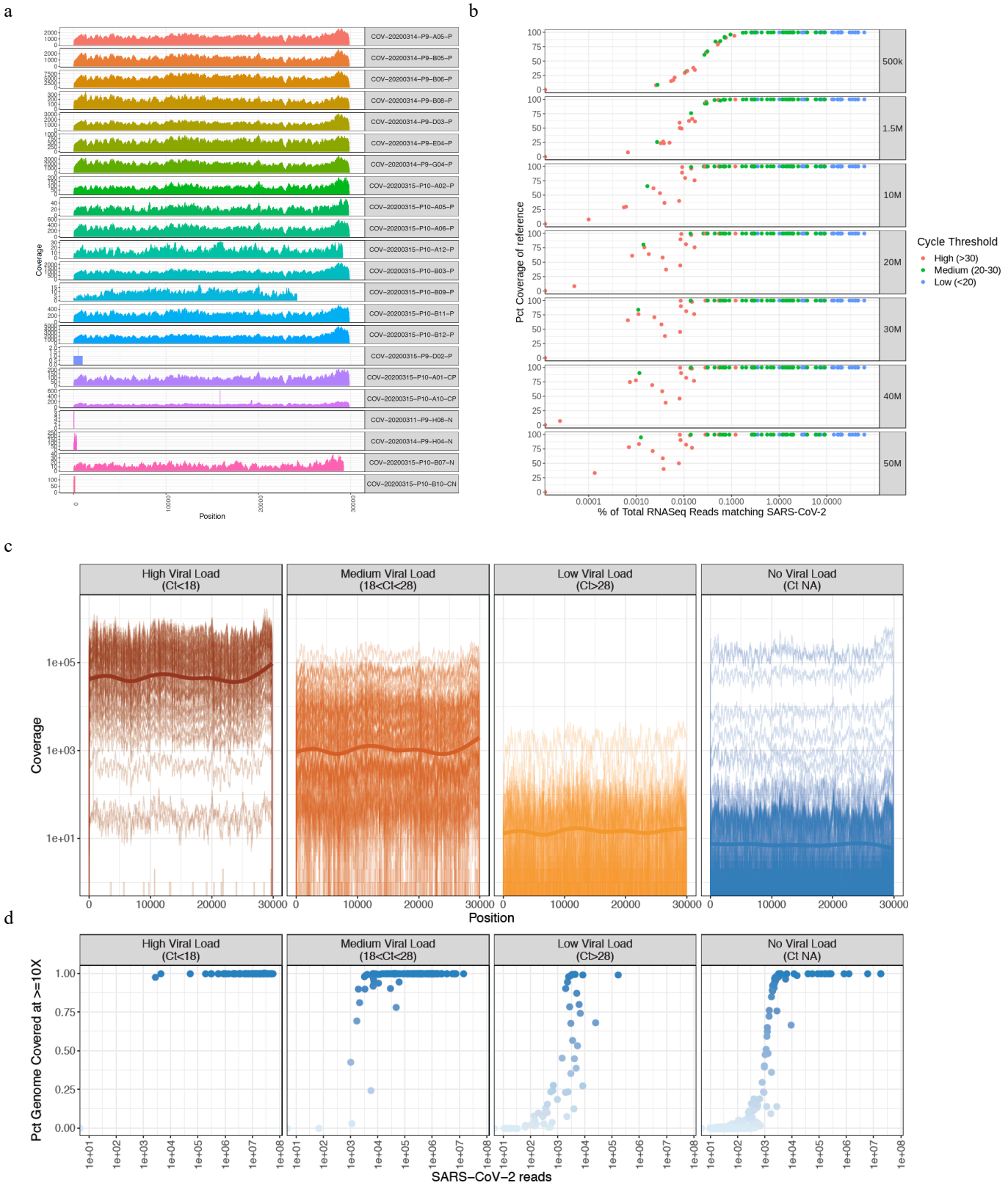


**Supplementary Figure 6. Viral genomes from RNA-seq data and titration of coverage** (a) The coverage plot across the SARS-CoV-2 genomes (viral coordinate on bottom, colored by sample) from a representative set of clinical positive samples. Sample names with the suffixes CN and N are clinical negative (buffer), P are qRT-PCR positive, and CP are Vero E6 cells with virus. (b) Downsampling (right annotation) of the samples and mapping to the SARS-CoV-2 genome to gauge the percent coverage (y-axis) as a function of the viral quantification by qRT-PCR (Ct thresholds, low <20, medium 20-30, and high>30). (c) Average coverage statistics for the low, medium, and high Ct samples, as well as the mean coverage for each of these samples. (d) The cycle threshold (x-axis) vs. the coverage of the genome (y-axis and color depth) for the total RNA-seq.

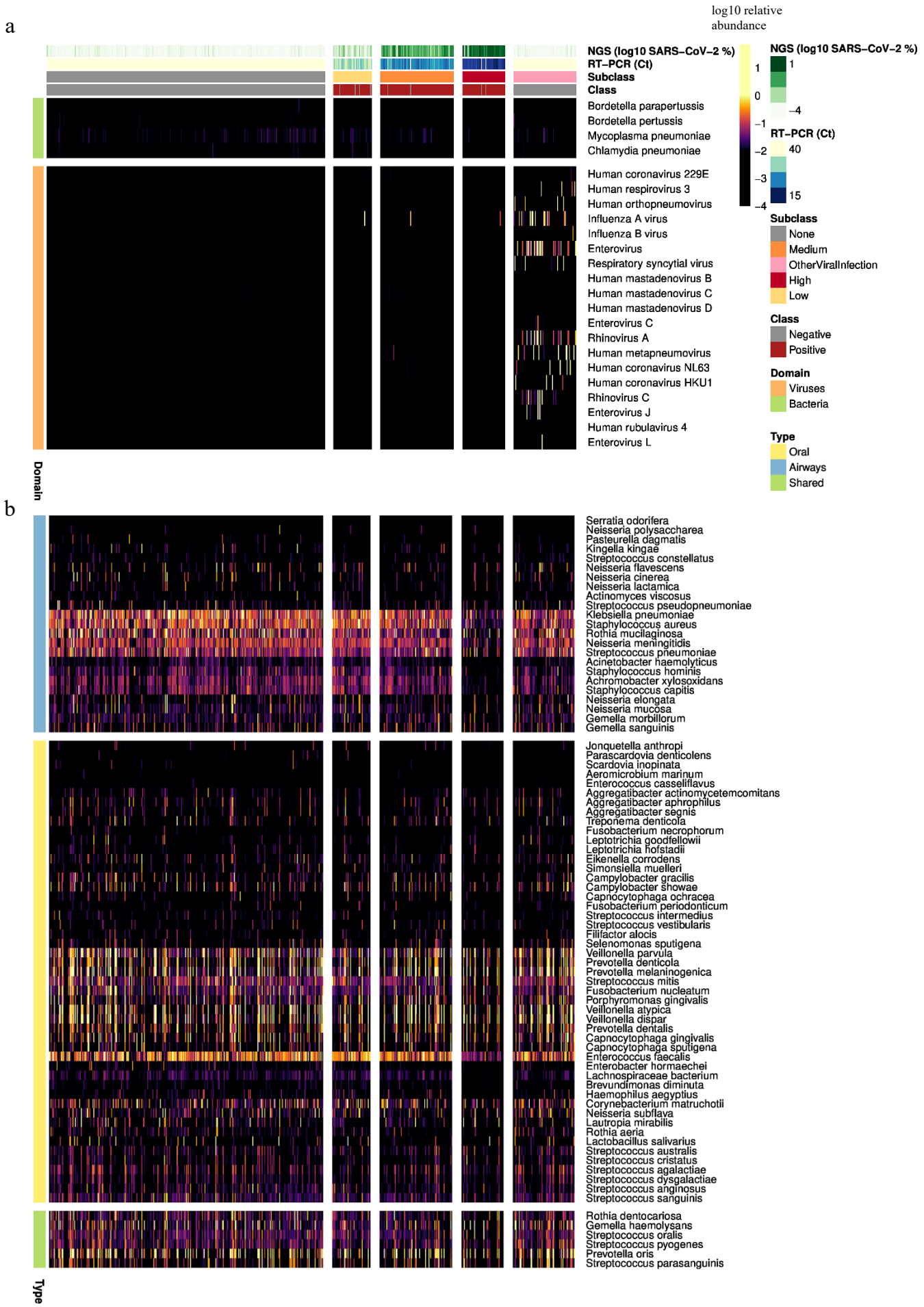
a
log10 relative abundance
NGS (log10 SARS−CoV−2 %)
RT−PCR (Ct)
Subclass
Class
Bordetella parapertussis
Bordetella pertussis
Mycoplasma pneumoniae
Chlamydia pneumoniae
Human coronavirus 229E
Human respirovirus 3
Human orthopneumovirus
Influenza A virus
Influenza B virus
Enterovirus
Respiratory syncytial virus
Human mastadenovirus B
Human mastadenovirus C
Human mastadenovirus D
Enterovirus C
Rhinovirus A
Human metapneumovirus
Human coronavirus NL63
Human coronavirus HKU1
Rhinovirus C
Enterovirus J
Human rubulavirus 4
Enterovirus L
Domain
1
0
−1
−2
−3
−4
NGS (log10 SARS−CoV−2 %)
1
−4
RT−PCR (Ct)
40
15
Subclass
None
Medium
OtherViralInfection
High
Low
Class
Negative
Positive
Domain
Viruses
Bacteria
Type
Oral
Airways
Shared
b
Serratia odorifera
Neisseria polysaccharea
Pasteurella dagmatis
Kingella kingae
Streptococcus constellatus
Neisseria flavescens
Neisseria cinerea
Neisseria lactamica
Actinomyces viscosus
Streptococcus pseudopneumoniae
Klebsiella pneumoniae
Staphylococcus aureus
Rothia mucilaginosa
Neisseria meningitidis
Streptococcus pneumoniae
Acinetobacter haemolyticus
Staphylococcus hominis
Achromobacter xylosoxidans
Staphylococcus capitis
Neisseria elongata
Neisseria mucosa
Gemella morbillorum
Gemella sanguinis
Jonquetella anthropi
Parascardovia denticolens
Scardovia inopinata
Aeromicrobium marinum
Enterococcus casseliflavus
Aggregatibacter actinomycetemcomitans
Aggregatibacter aphrophilus
Aggregatibacter segnis
Treponema denticola
Fusobacterium necrophorum
Leptotrichia goodfellowii
Leptotrichia hofstadii
Eikenella corrodens
Simonsiella muelleri
Campylobacter gracilis
Campylobacter showae
Capnocytophaga ochracea
Fusobacterium periodonticum
Streptococcus intermedius
Streptococcus vestibularis
Filifactor alocis
Selenomonas sputigena
Veillonella parvula
Prevotella denticola
Prevotella melaninogenica
Streptococcus mitis
Fusobacterium nucleatum
Porphyromonas gingivalis
Veillonella atypica
Veillonella dispar
Prevotella dentalis
Capnocytophaga gingivalis
Capnocytophaga sputigena
Enterococcus faecalis
Enterobacter hormaechei
Lachnospiraceae bacterium
Brevundimonas diminuta
Haemophilus aegyptius
Corynebacterium matruchotii
Neisseria subflava
Lautropia mirabilis
Rothia aeria
Lactobacillus salivarius
Streptococcus australis
Streptococcus cristatus
Streptococcus agalactiae
Streptococcus dysgalactiae
Streptococcus anginosus
Streptococcus sanguinis
Rothia dentocariosa
Gemella haemolysans
Streptococcus oralis
Streptococcus pyogenes
Prevotella oris
Streptococcus parasanguinis
Type

**Supplemental Figure 7. Metatranscriptome profiles of the patient cohorts.** (top row, all panels) Samples were quantified by a range of viral detection methods, including RNA-seq (log10 SARS-CoV-2 % of reads) and qRT-PCR (Ct values) to create a three-tier range of viral load for the positive samples (right) compared to the clinically-annotated negative samples (class, red or grey). (bottom) The detected microbial species (horizontal lines) are plotted as log10 abundance. (a) Common respiratory pathogens plotted as a $\log_{10}$ abundance of mapped reads, with each organism as a line and each vertical column as a patient. (b) The same layout of samples as (a), but with bacteria annotated from the Human Microbiome Project (HMP) as normal airway (blue, top portion), oral (yellow, middle set), or both oral and airway flora (green, bottom).

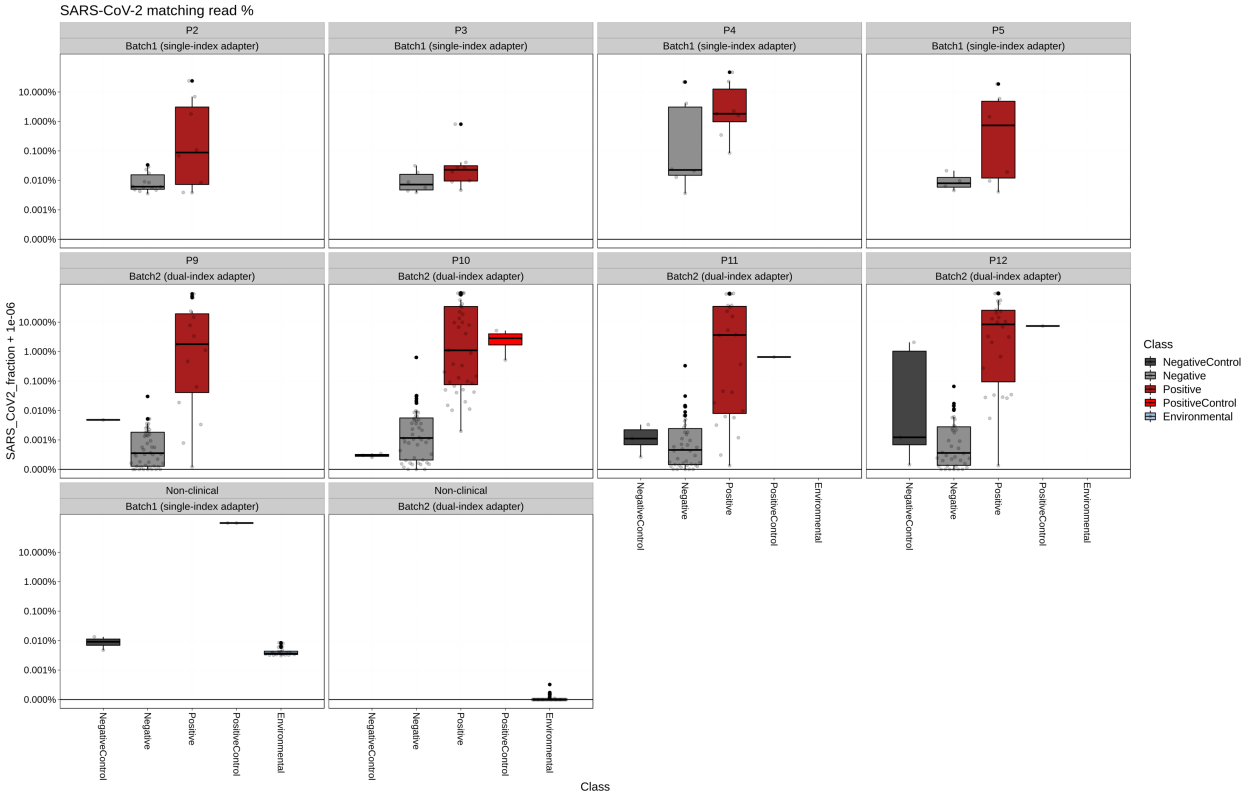


**Supplemental Figure 8. Proportion of RNA-seq reads mapping SARS-CoV-2.** Clinical samples tested by qRT-PCR (Positive, dark red or Negative, light grey) were sequenced and compared to the buffer blanks (Negative Control), dark grey, Synthetic RNAs or Vero 6 cell extracts with SARS-CoV-2 infection (Positive Controls, light red), and Subway Samples (Environmental, blue). Read totals are shown on the y-axis. Differences between single index barcodes are plotted across each of the plates of samples that were processed.

a

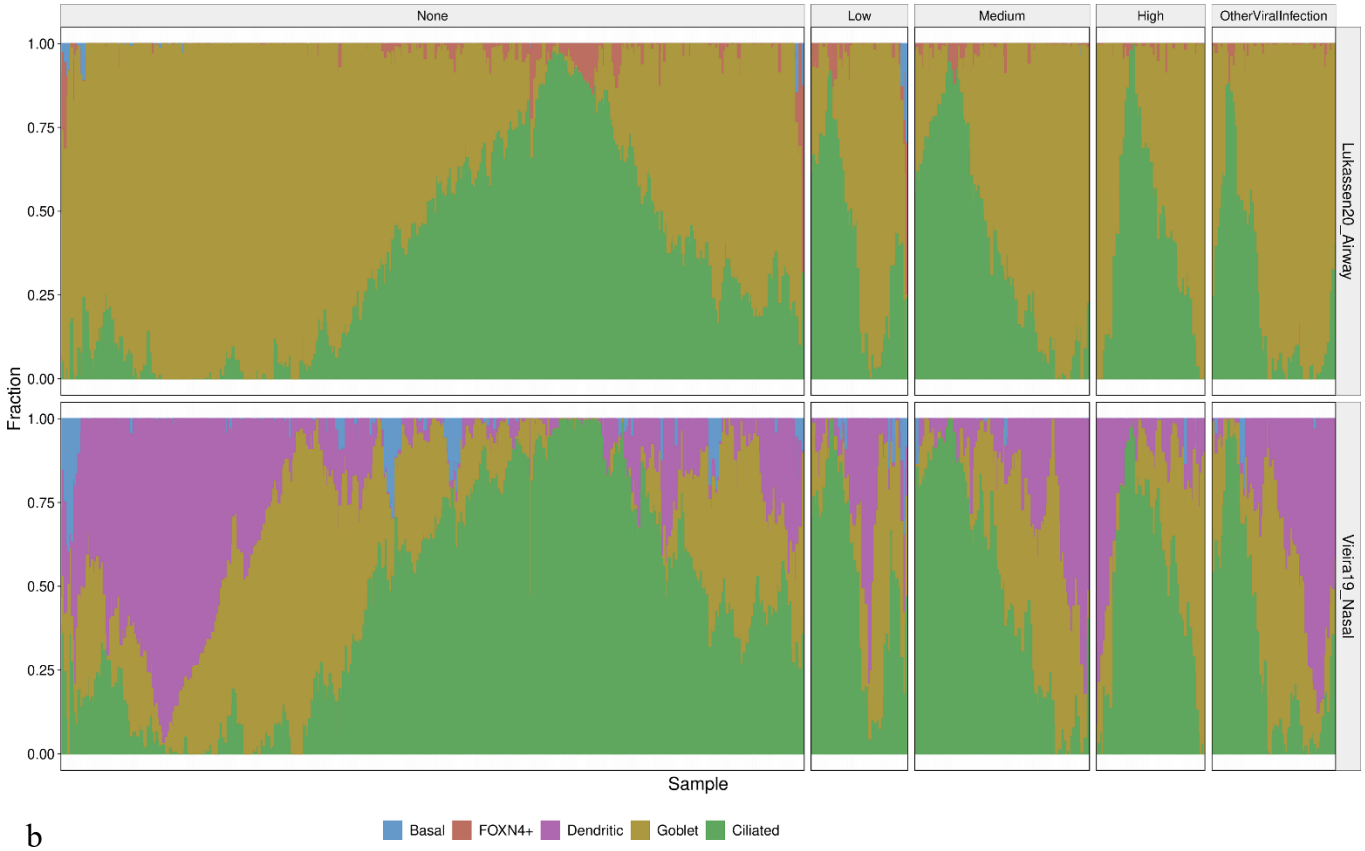
None
Low
Medium
High
OtherViralInfection
Lukassen20_Airway
Vieira19_Nasal
Fraction
1.00
0.75
0.50
0.25
0.00
Sample
Basal
FOXN4+
Dendritic
Goblet
Ciliated

b

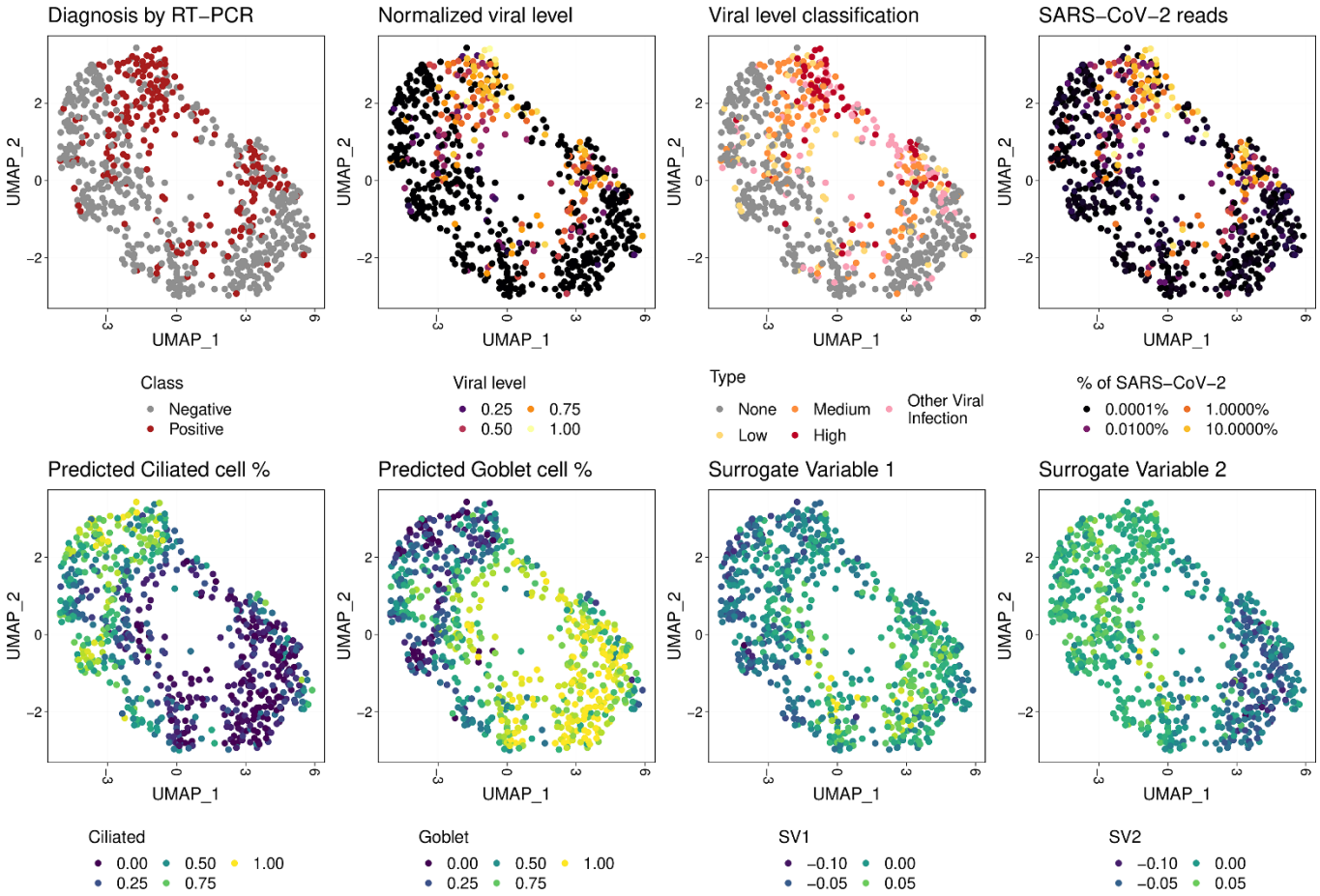
Diagnosis by RT−PCR
Normalized viral level
Viral level classification
SARS−CoV−2 reads
UMAP_1
UMAP_2
Class
Negative
Positive
Viral level
0.25
0.50
0.75
1.00
Type
None
Low
Medium
High
Other Viral Infection
% of SARS−CoV−2
0.0001%
0.0100%
1.0000%
10.0000%
Predicted Ciliated cell %
Predicted Goblet cell %
Surrogate Variable 1
Surrogate Variable 2
Ciliated
Goblet
SV1
SV2
−0.10
−0.05
0.00
0.05

**Supplemental Figure 9. Cellular sub-type deconvolution from nasopharyngeal (NP) swabs.** The MUSIC algorithm was used to separate the cellular sub-type gene expression signatures present in the total RNA-seq data from the NP swabs. (a) The fraction of cells estimated for each cell type (y-axis) was calculated for the clinical samples that tested positive by RT-qPCR in different viral levels, as well as negative by RT-qPCR, with proportions shown for goblet cells (yellow), ciliated cells (green), basal cells (blue), dendritic cells (purple) and FOXN4+ cells (red). First row shows deconvolution using the single cell transcription reference set of upper airway cells by Lukassen *et al* 2020. and the second row shows a similar approach using nasal epithelial cells by Vieria *et al*. (b) Clinical samples are embedded in two-dimensions using dimensionality reduction by UMAP and separate features of samples are projected onto the points including RT-PCR based diagnosis, viral levels, fraction of SARS-CoV-2 reads as captured by NGS, predicted ciliated and goblet cell fractions from cell deconvolution using Lukassen airway reference, and the two predicted surrogate variables.

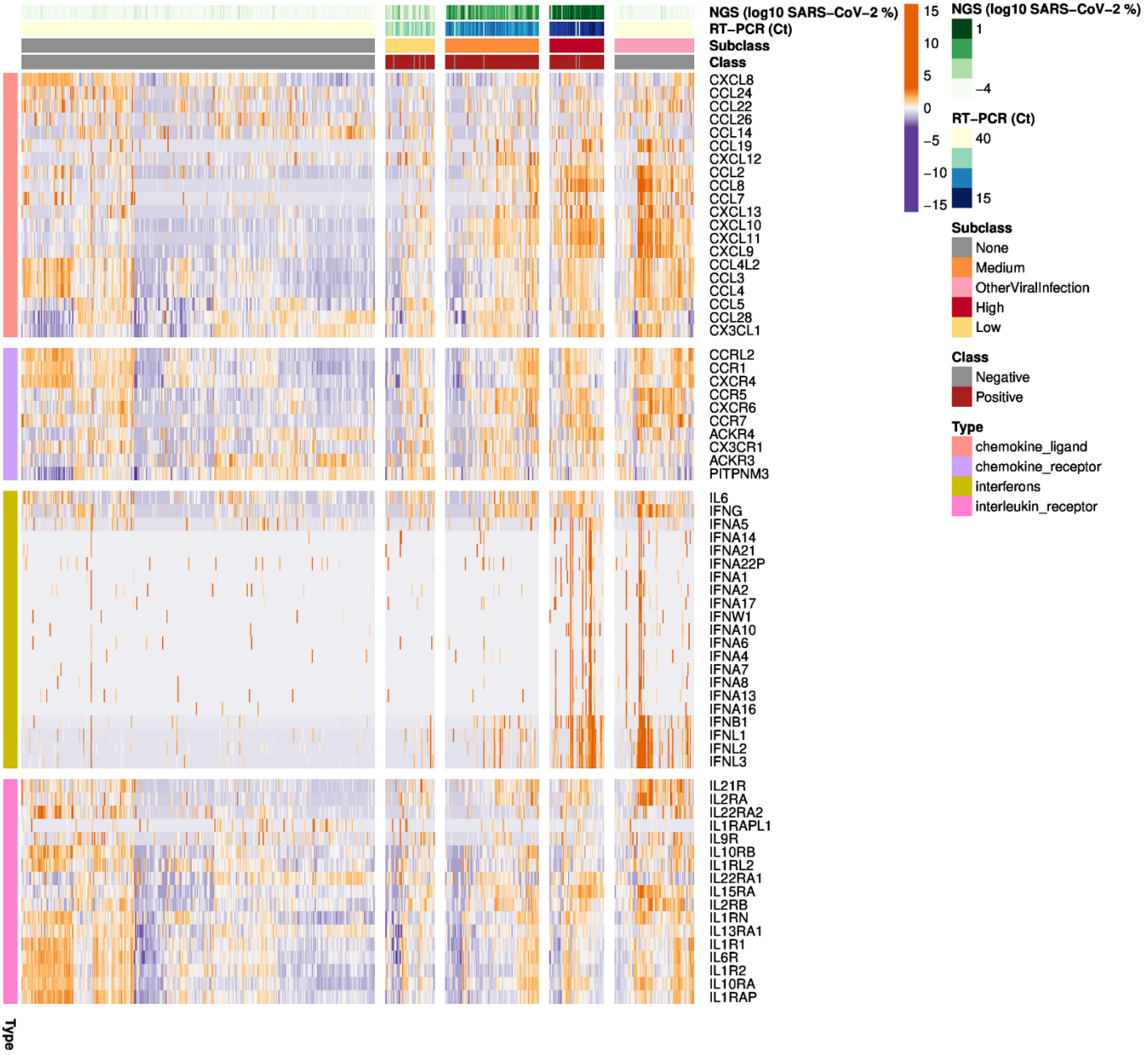


**Supplemental Figure 10. Cytokine and interferon profiles of the host transcriptome.** Top rows: samples were quantified by a range of viral detection methods, including LAMP (QuantiFluor), RNA-seq (log10 SARS-CoV-2 % of reads), and qRT-PCR (Ct values) to create a three-tier range of viral load for the positive samples (right) compared to the clinically-annotated negative samples (class, red or grey). (bottom) The differentially expressed genes of SARS-CoV-2

positive patients compared to SARS-CoV-2 negative patients showed up-regulated (orange) genes as well as down-regulated (purple) genes. Heatmap is separated into Chemokine ligand, chemokine receptor, interferon and interleukin receptor profiles for the samples (x-axis) is plotted for each related gene (y-axis).

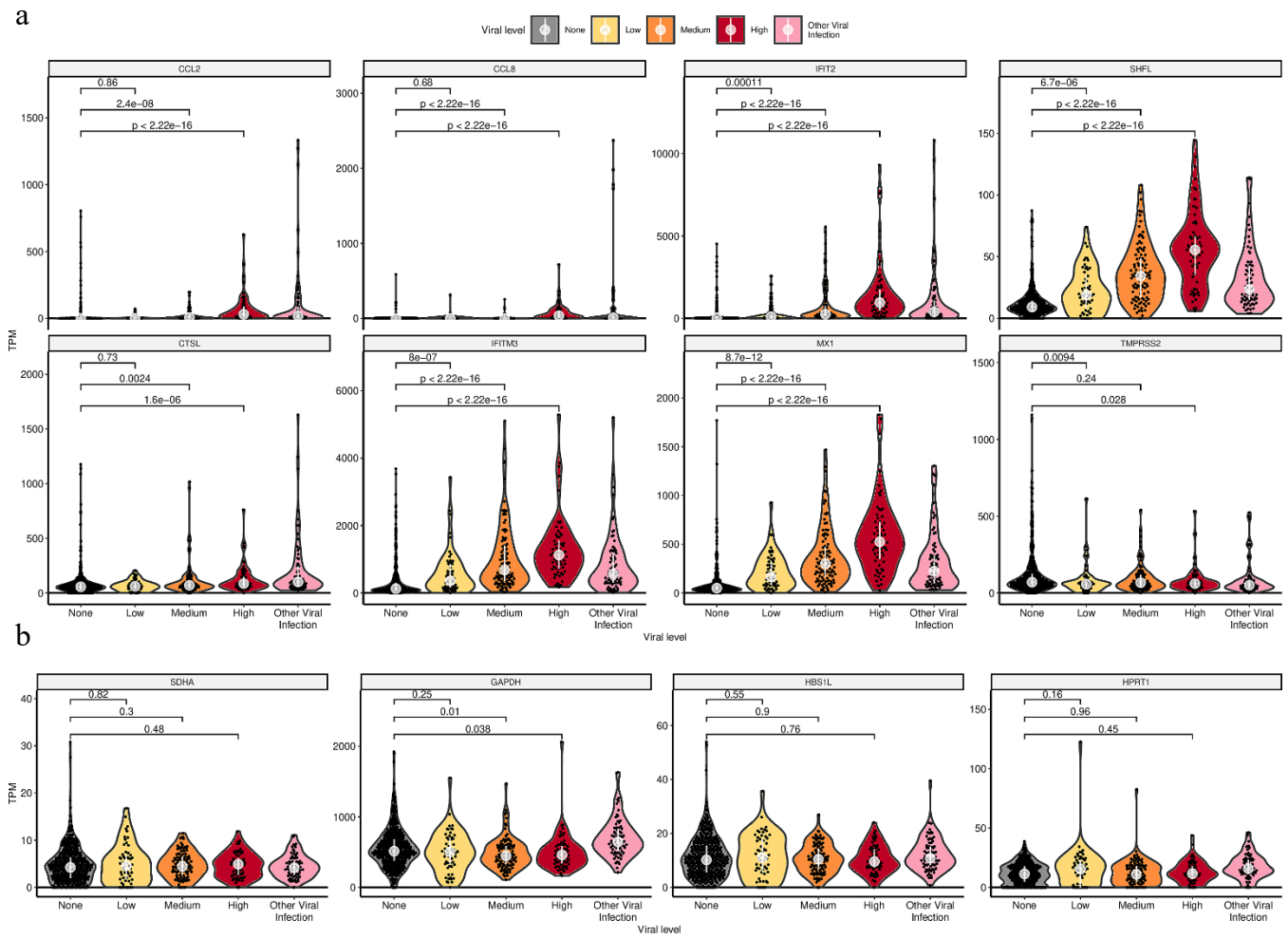


**Supplemental Figure 11. Host gene expression relative to SARS-CoV-2 infection.** Clinical samples were sequenced with RNA-seq and quantified to a set of genes for their expression levels. Samples with no virus (grey) were compared to those with low (yellow), medium (orange), and high (red) expression levels, based on qRT-PCR. p-values are calculated by Wilcoxon rank sum test and are not adjusted for multiple testing for a given gene. (a) Additional genes that were differentially expressed, or reported to be important for SARS-CoV-2 entry. (b) Expression of housekeeping genes in different groups.

a

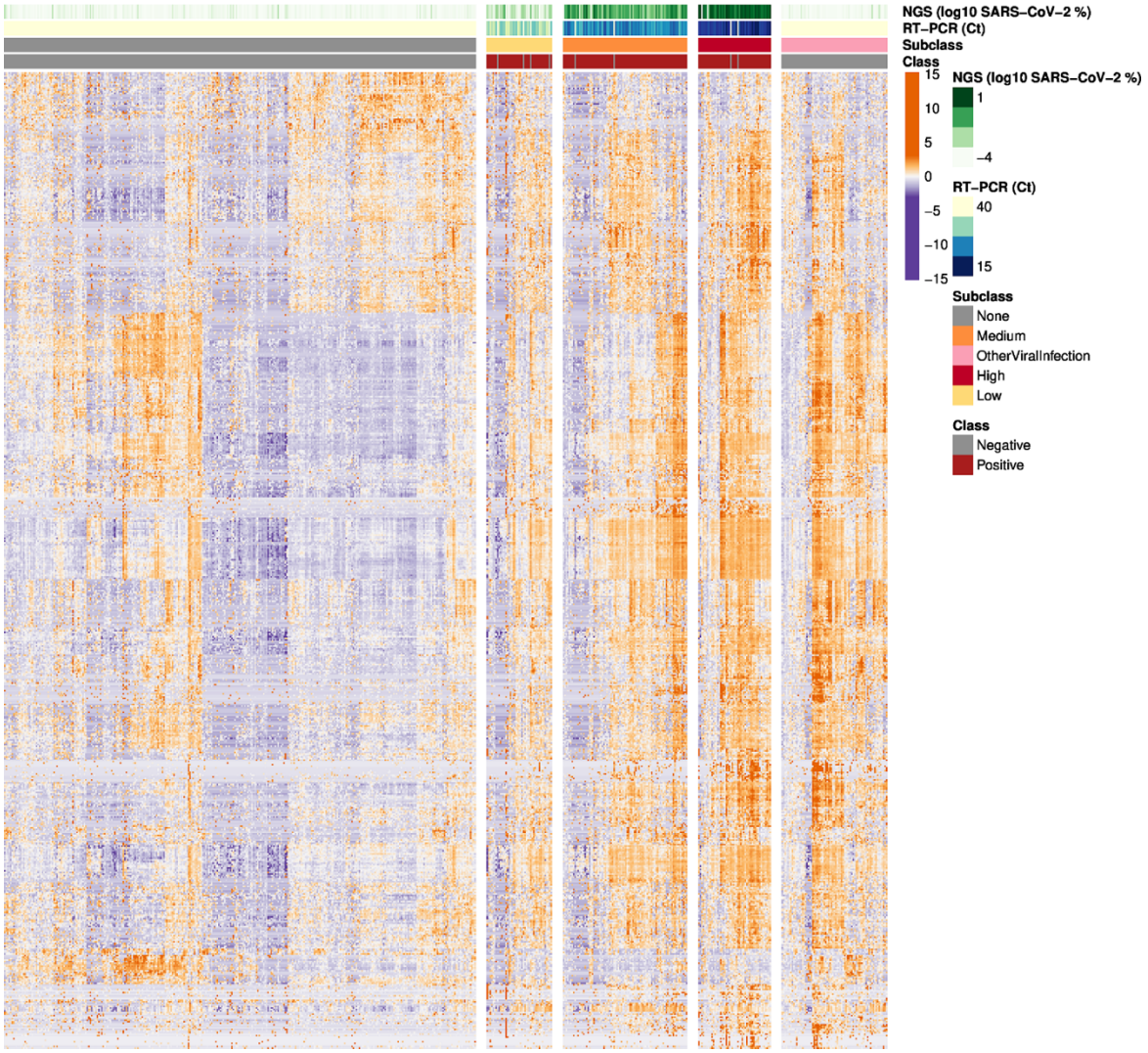
NGS (log10 SARS−CoV−2 %)
RT−PCR (Ct)
Subclass
Class
15
10
5
0
−5
−10
−15
NGS (log10 SARS−CoV−2 %)
1
−4
RT−PCR (Ct)
40
15
Subclass
None
Medium
OtherViralInfection
High
Low
Class
Negative
Positive

b

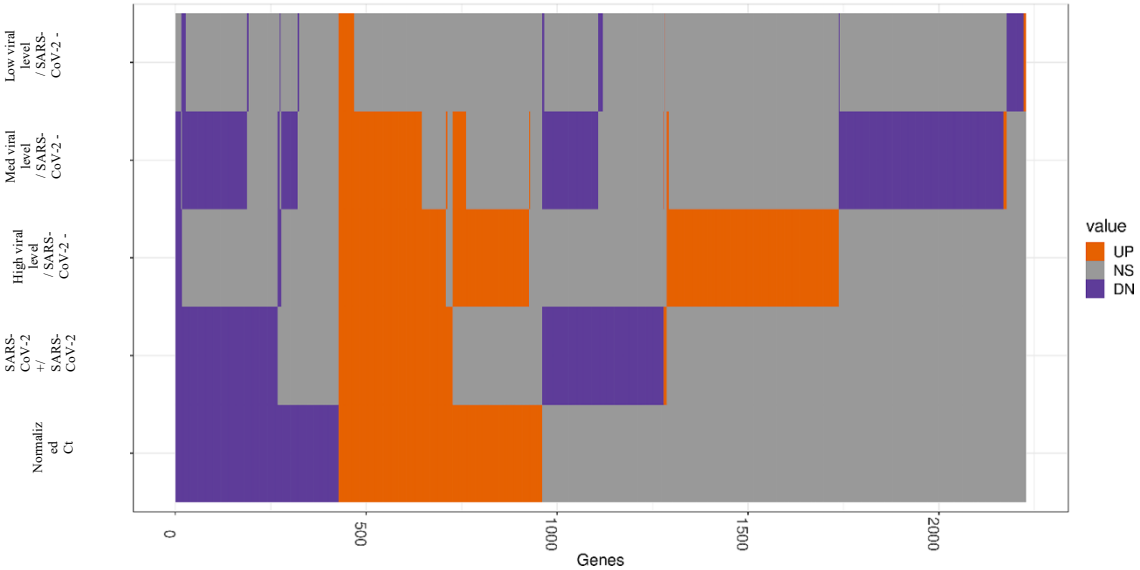
Low viral level / SARS-CoV-2 -
Med viral level / SARS-CoV-2 -
High viral level / SARS-CoV-2 -
SARS-CoV-2 +/ SARS-CoV-2
Normalized Ct
0
500
1000
1500
2000
Genes
value
UP
NS
DN

**Supplemental Figure 12. Differentially expressed genes.** (a) Top rows: samples were quantified by a range of viral detection methods, including LAMP (QuantiFluor), RNA-seq (log10 SARS-CoV-2 % of reads), and qRT-PCR (Ct values) to create a three-tier range of viral load for the positive samples (right) compared to the clinically-annotated negative samples (class, red or grey). (bottom) The differentially expressed genes of SARS-CoV-2 positive patients compared to SARS-CoV-2 negative patients showed up-regulated (orange) genes as well as down-regulated (purple) genes. All differentially expressed genes with adjusted p-value < 0.001 and |log2 fold-change| > 1.5 (> 2.82 fold) are shown across different patient groups by viral level and presence of other viral pathogens. (b) Intersection heatmap of differentially expressed genes across different comparisons with genes in x-axis and comparisons in y-axis, with a core set of up-regulated genes (orange) distinct form the set of down-regulated genes (purple), compared to genes that are not significantly differently expressed (grey) in any comparison (Limma voom, q-value <0.01, |log2FC| >0.58).

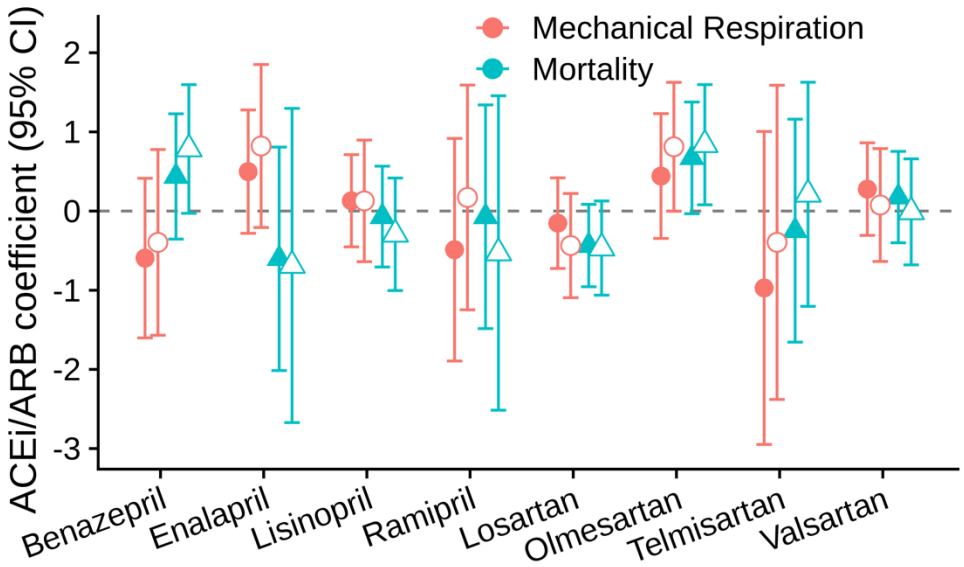


**Supplemental Figure 13. ACEI/ARBs Multivariate and Comparative Analyses.** Comparison of the effects of different ACEIs (benazepril, enalapril, lisinopril, ramipril) and ARBs (losartan, olmesartan, telmisartan, valsartan) when compared to patients exposed to other ACEIs or ARBs, respectively. There were no significant findings amongst the different ACEIs. However, among the ARBs we found that olmesartan was associated with a significant increase in mortality (HR=2.3 CI: 1.1-4.9, p=3.05E-02).

**Supplementary Table 1. Metatranscriptome Profiles of All Samples.**
Appended.

**Supplementary Table 2. Taxonomic Mis-assignment Filter.**
Appended.

**Supplementary Table 3. Differentially Expressed Genes in SARS-CoV-2 +/- patients.** Appended.

**Supplemental Table 4. Gene Ontology Pathways.**
Appended.

**Supplementary Table 5. SARS-CoV-2 Rapid Colorimetric LAMP Detection Test: N Primers Specificity**
Appended.

**Supplementary Table 6. Logistic Regression Coefficient**
Appended.

**Supplementary Table 7. Hypertension Logistic Regression Coefficient**
Appended.

**Supplementary Table 8. COX Regression Coefficients**
Appended.

**Supplementary Table 9. Hypertension COX Regression Coefficients**
Appended.

**Supplementary Table 10: GISAID COVID-19 Acknowledgments**
Appended.